Fuel 419 (2026) 138864

Contents lists available at ScienceDirect

Fuel

journal homepage: www.elsevier.com/locate/fuel

Full Length Article

Integrated Wind-Solar-LNG system for green liquefied hydrogen and multi-energy supply: Techno-Economic-Environmental analysis and data-driven ANN-GA optimization

Ling Ji [a], Ali Basem [b], Hyder H. Abed Balla [c,*], Omar J. Alkhatib [d,*], Khalid Alkhattabi [e], Yonghui Li [f,*], M.A. Ahmed [g,*], Mohana Alanazi [h], Hind Albalawi [i], Ibrahim Mahariq [j,k,l,m,n,**]

[a] School of Logistics, Linyi University, Linyi 276000, China
[b] Advanced Technical College, University of Warith Al-Anbiyaa, Karbala, Iraq
[c] Aeronautical Technical Department, Najaf Technical Institute,Al Furat Al Awsat Technical University, Najaf, Kufa, Iraq
[d] Architectural Engineering Department, United Arab Emirates University Al Ain, United Arab Emirates
[e] College of Computers and Information Technology, University of Tabuk, Tabuk 47512, Saudi Arabia
[f] School of Digital Economy and Management, Sichuan University of Technology and Business, Meishan, Sichuan 620000, China
[g] Department of Mathematics, College of Science, Majmaah University, Al-Majmaah 11952, Saudi Arabia
[h] Department of Electrical Engineering, College of Engineering, Jouf University, Sakaka 72388, Saudi Arabia
[i] Department of Physics, College of Sciences, Princess Nourah bint Abdulrahman University, P.O. Box 84428, Riyadh 11671, Saudi Arabia
[j] College of Engineering and Architecture, Gulf University for Science and Technology, Mishref, Kuwait
[k] Department of Electrical and Electronic Engineering, Faculty of Engineering and Architecture, Istanbul Gelisim University, Avcılar- Istanbul, 34310, Istanbul, Türkiye
[l] Najjad Zeenni Faculty of Engineering, Al-Quds University, Jerusalem, Palestine
[m] Department of Medical Research, China Medical University Hospital, China Medical University, Taichung, Taiwan
[n] University College, Korea University, Seoul 02481, South Korea

ARTICLE INFO

Keywords:
District-scale energy systems
Hydrogen liquefaction
LNG cold energy
Techno-economic optimization
Wind–solar cogeneration

ABSTRACT

The production of low-carbon hydrogen fuel is critical for sustainable energy systems. This study proposes a centralized district-scale wind–solar cogeneration system designed to generate green liquefied hydrogen alongside electricity, cooling, and freshwater for zero-emission building clusters. The system couples a wind farm and parabolic trough solar collectors with an LNG regasification unit, steam and organic Rankine cycles, an absorption refrigeration cycle, a thermoelectric generator, a reverse osmosis desalination plant, a proton exchange membrane electrolyzer, and a Claude-based hydrogen liquefaction cycle. LNG cold energy is strategically utilized to enhance hydrogen liquefaction efficiency, reduce refrigeration energy demand, and maximize overall exergy utilization. Cascaded thermal integration among power, cooling, and hydrogen subsystems further improves waste-heat recovery and system performance. A comprehensive energy, exergy, economic, and environmental assessment is conducted, and multi-objective optimization using NSGA-II, assisted by an artificial neural network surrogate model (MSE = 0.00681), substantially reduces computational time while maintaining high accuracy. Under optimal conditions, the system achieves an exergy efficiency of 21.25%, producing 4.19 kg/h of liquefied hydrogen as a green fuel, 1.39 MW of net electricity, and freshwater and cooling at a 29.6% lower total cost rate relative to the baseline. A case study for Dammam, Saudi Arabia, demonstrates the system's potential as a scalable, low-carbon, integrated energy–water–fuel solution in hot-arid climates.

1. Introduction

Achieving net-zero energy performance in modern buildings has become a key priority in sustainable urban planning [1]. This shift is driven by rapid growth in energy demand, increasing environmental pressures, and the need for reliable long-term energy supply [2,3]. Conventional fossil-fuel-based infrastructures are increasingly

* Corresponding authors.
** Corresponding author at: Najjad Zeenni Faculty of Engineering, Al-Quds University, Jerusalem, Palestine.
E-mail addresses: hyderballa@atu.edu.iq (H.H. Abed Balla), omar.alkhatib@uaeu.ac.ae (O.J. Alkhatib), gytfb588@126.com (Y. Li), moh.hassan@mu.edu.sa (M.A. Ahmed), Ibmahariq@gmail.com (I. Mahariq).

https://doi.org/10.1016/j.fuel.2026.138864
Received 22 December 2025; Received in revised form 31 January 2026; Accepted 18 February 2026
Available online 25 February 2026

Nomenclature

Symbols

A	Area (m^2)
$C_{P,wt}$	Power coefficient of wind turbine
e_{CO_2}	Natural gas emission factor (kg/kWh)
ERC	Emission reduction cost $(\$/h)$
$\dot{E}x$	Exergy rate (kW)
ex	Specific exergy (kJ/kg)
F	Faraday constant (C/mol)
G	Solar irradiation (W/m^2)
h	Specific enthalpy (kJ/kg)
J	Current density (A/m^2)
k	Thermal conductivity (kW/m)
$\dot{m}$	Mass flow rate (kg/s)
P	Pressure (kPa)
PR	Pressure ratio
$\dot{Q}$	Heat transfer rate (kW)
R	Gas constant $(kJ/kg.K)$
s	Specific entropy $(kJ/kg.K)$
T	Temperature $(^{\circ}C)$
U	Heat transfer coefficient $(kW/m^2.K)$
V	Voltage (V)
V_w	Average wind speed (m/s)
$\dot{W}$	Power rate (kW)
$\dot{Z}$	Cost rate $(\$/h)$
ΔG	Change in Gibbs free energy (kJ)

Greek Symbols

η	Efficiency
λ	Water content in PEME
σ	Spatially resolved ionic conductivity
φ	Maintenance factor

Subscripts

1,2, …	State points
a	Anode
act	Actual
c	Cathode
ch	Chemical
cond	Condenser
fw	Freshwater
in	Inlet stream
is	Isentropic
ohm	Ohmic
out	Outlet stream
ph	Physical
PT	Pelton turbine
tur	Turbine
wt	Wind turbine

Abbreviations

ANN	Artificial neural network
ARC	Absorption refrigeration cycle
CRF	Capital recovery factor
HEX	Heat exchanger
LCOH	Levelized cost of hydrogen
LINMAP	Linear programming technique for multidimensional analysis of preference
LNG	Liquefied natural gas
NPV	Net present value
NSGA −II	Non-dominated sorting genetic algorithm II
ORC	Organic Rankine cycle
PEME	Proton exchange membrane electrolyzer
PTCS	Parabolic through solar collector
RO	Reverse osmosis
SRC	Steam Rankine cycle
TEG	Thermoelectric generator

unsuitable for this role due to resource depletion and high greenhouse gas emissions [4,5]. As a result, renewable-driven district-scale energy systems have gained attention as practical solutions for supplying multiple energy services in an efficient and coordinated manner [6–8].

Among available renewable options, hybrid wind–solar systems offer enhanced reliability compared to single-source configurations, owing to the complementary nature of solar irradiance and wind availability [9–11]. When integrated within cogeneration or multi-generation platforms, these hybrid systems can simultaneously deliver electricity, cooling, water, and fuels while achieving higher overall energy utilization through structured waste-heat recovery [12–14]. Such integrated architectures are particularly attractive for net-zero building districts, where diverse and continuous energy services must be supplied with minimal environmental impact [15,16].

Modern urban districts increasingly require electricity, cooling, freshwater, and access to low-carbon fuels such as hydrogen [17,18]. Supplying these demands through independent conventional systems often leads to excessive fuel consumption, reduced efficiency, and increased environmental impacts [19,20]. As a result, integrated renewable-based multi-generation systems have emerged as high-performance alternatives [21]. By combining renewable energy sources with advanced thermodynamic cycles and structured waste-heat recovery, these systems enable the simultaneous production of multiple outputs with improved energy and exergy efficiencies [22–24]. Such coordinated utilization of thermal and electrical resources reduces operational costs and emissions, offering a technically and environmentally sound pathway for meeting the complex energy needs of net-zero building districts [25,26].

A growing body of research has focused on improving renewable-powered multi-generation configurations. Zhang et al. [27] proposed an advanced operational framework for a hybrid solar–wind system incorporating storage and hydrogen production. This method lowered operating expenditures by 16.22% while raising renewable utilization to 80–95%, ultimately improving both economic outcomes and overall system performance. Assareh et al. [28] examined a solar–wind multi-generation system for residential applications in hot climates, integrating a modified steam Rankine cycle (SRC) and reverse osmosis (RO) desalination. The system delivered electricity, heating, cooling, and freshwater with energy and exergy efficiencies of 33–34%, achieved a CO_2 reduction of 1,334 ton, and demonstrated net-zero energy capability, supplying surplus energy back to the grid. Imandoust et al. [29] optimized a solar–wind-assisted system for electricity and freshwater production. Using the NSGA-II optimization algorithm, they improved energy and exergy efficiencies to 42.64% and 40.32%, respectively, while achieving outputs of 61.56 MW of electricity and 3,246 m^3/h of freshwater. These studies confirm the strong potential of renewable-driven multi-generation systems, while also highlighting the growing complexity of integrated designs.

In parallel, hydrogen has emerged as a critical component of future low-carbon energy frameworks due to its ability to function as a clean and flexible energy carrier [30–32]. Its role in decarbonizing power generation, industry, and transportation positions hydrogen as a key enabler of large-scale renewable energy deployment [33,34]. Among available production routes, renewable-powered water electrolysis offers the most environmentally benign option, avoiding the carbon intensity associated with fossil-based methods. Proton exchange

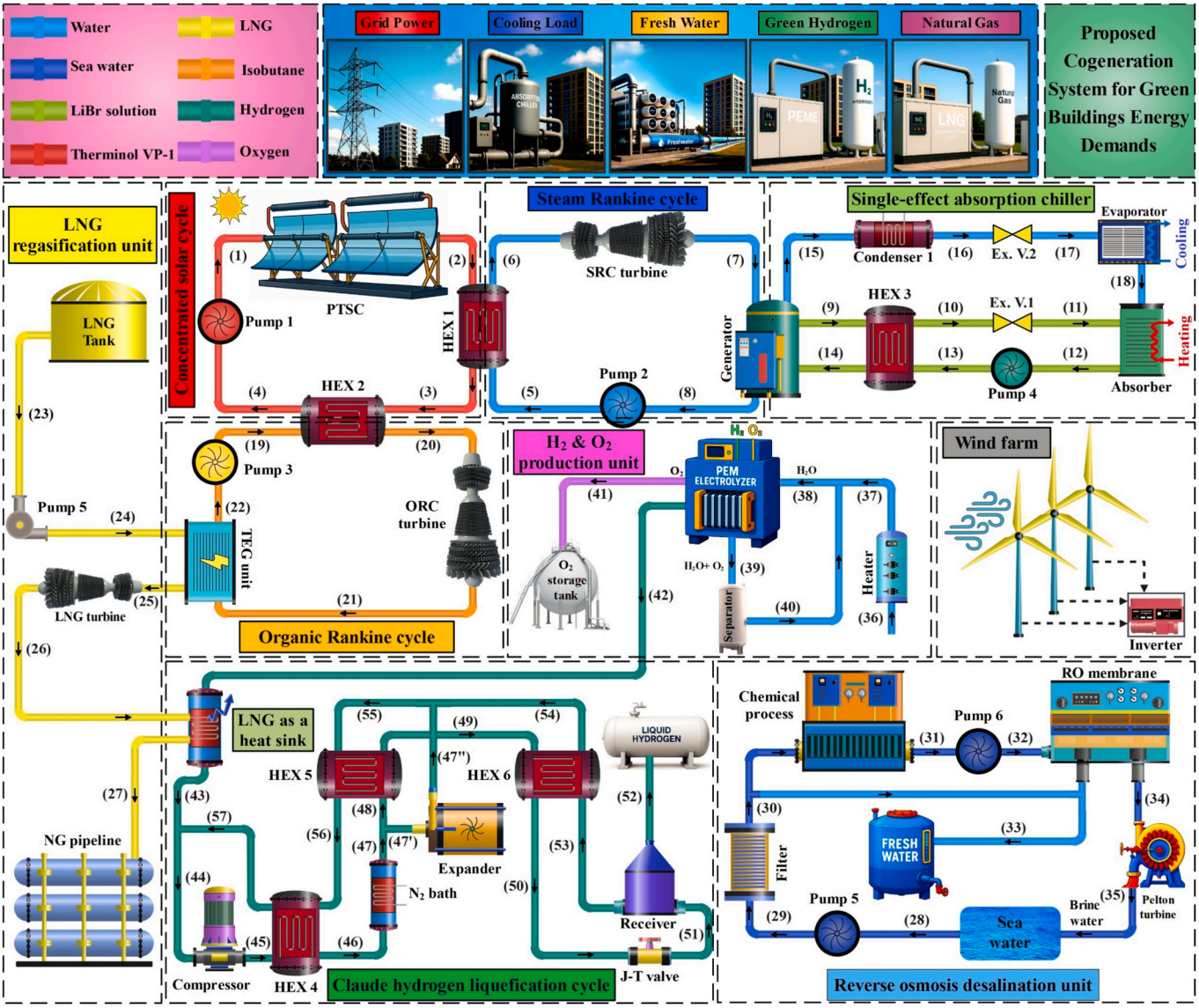

Fig. 1. Conceptual layout of the proposed renewable-based multi-generation system.

membrane electrolyzers (PEMEs) have attracted particular attention due to their high efficiency, rapid dynamic response under fluctuating renewable inputs, and compact design [35]. However, despite advances in production technologies, hydrogen storage remains a major barrier to large-scale implementation [36]. Owing to hydrogen's low volumetric energy density, advanced storage approaches, including high-pressure compression, chemical carriers, and cryogenic liquefaction have been investigated [37]. Among these options, hydrogen liquefaction provides significantly increased volumetric density and improved suitability for long-distance transport and large-scale storage, making it a promising solution for future multi-energy systems [38].

Recent studies have explored multi-generation systems incorporating hydrogen production and liquefaction. Hai et al. [39] introduced an integrated system that couples a solid oxide fuel cell with a water electrolyzer and a Claude liquefaction cycle, enabling simultaneous hydrogen generation and cryogenic storage. In another study, Qing et al. [40] examined a solar-assisted multi-generation arrangement incorporating a proton exchange membrane electrolyzer (PEME) and a Claude hydrogen liquefier. Their optimization and sensitivity investigations raised hydrogen production to 33.53 kg/h, while also supplying electricity and cooling, supported by comprehensive techno-economic and environmental evaluations. Similarly, Wei et al. [41] developed a solar-driven configuration integrating a solid oxide electrolyzer with a Claude cycle, demonstrating favorable thermodynamic and economic performance. While these studies highlight the feasibility of hydrogen-integrated systems, most remain focused on individual components or limited-service outputs.

The inherently integrated nature of multi-generation systems introduces significant design complexity, requiring the simultaneous consideration of technical performance, economic viability, and environmental impacts [42]. Conventional optimization approaches often struggle under this complexity, leading to high computational cost and long execution times [43]. To overcome these limitations, surrogate-based optimization methods, particularly those combining artificial neural networks (ANNs) with multi-objective optimization algorithms have gained increasing attention [44]. Previous studies have demonstrated that ANN-based surrogate models can significantly reduce computational effort while maintaining high predictive accuracy [45–48]. Nevertheless, their application to district-scale hybrid wind–solar cogeneration systems incorporating hydrogen liquefaction and liquefied natural gas (LNG) regasification remains limited.

Despite significant advances in renewable energy technologies,

existing solutions remain limited in their ability to reliably supply multiple energy services to net-zero building districts. First, while hybrid wind-solar systems are recognized, their integration within a single cogeneration framework designed explicitly for net-zero building districts, simultaneously providing power, cooling, water, and storable fuel needs more attention. Second, the potential of liquefied natural gas (LNG) regasification as a dual-purpose sink (providing cooling for hydrogen liquefaction and supplying pipeline gas) within such a renewable system is largely untapped. Third, the integration of green hydrogen liquefaction into building-scale energy systems, especially using recovered cold energy, lacks comprehensive techno-economic-environmental assessment. Finally, the operational optimization of such complex systems under real climatic conditions requires efficient computational strategies, such as surrogate-based models.

To address these challenges, this study introduces a fully integrated hybrid wind–solar cogeneration system tailored to the multi-faceted energy demands of net-zero green building districts. The proposed configuration simultaneously delivers electricity, cooling, freshwater, residential-grade natural gas, and liquefied hydrogen through an interconnected set of thermodynamic cycles. The system incorporates wind turbines, parabolic trough solar collectors (PTSCs), an LNG regasification unit, an SRC coupled with a single-effect absorption refrigeration cycle (ARC), an organic Rankine cycle (ORC) coupled with a thermoelectric generator (TEG), an RO desalination system, a PEME, and a Claude-based hydrogen liquefaction process. Renewable-generated electricity is converted to hydrogen, while both system-generated waste heat and LNG cryogenic exergy are strategically harnessed to improve liquefaction efficiency. The regasification process concurrently supplies additional power and provides natural gas suitable for building use, reinforcing the system's role as a multi-service urban energy solution. The developed modeling and optimization framework is general and can be applied to other geographical contexts by utilizing local meteorological and economic data. The core contributions of the present study are presented as follows:

- **Development of a district-scale hybrid wind–solar cogeneration system** supplying electricity, cooling, freshwater, natural gas, and liquefied hydrogen.
- **Novel integration of LNG regasification as a cryogenic sink** to enhance hydrogen liquefaction efficiency while providing additional power and usable natural gas.
- **Incorporation of liquefied green hydrogen** as a long-duration energy storage medium to improve renewable utilization and system flexibility.
- **Deployment of advanced waste-heat recovery strategies,** including SRC–ARC coupling and ORC–TEG integration.
- **Comprehensive 4E performance assessment** suitable for district-scale applications.
- **Implementation of an ANN-based surrogate framework coupled with NSGA-II** to reduce computational cost of multi-criteria optimization.
- **Demonstration of real-world feasibility** for hot-arid regions through a case study in Dammam, Saudi Arabia.

2. System description

Fig. 1 illustrates a centralized hybrid wind–solar cogeneration system developed to meet the integrated energy demands of net-zero green building districts. The system is engineered to simultaneously supply electricity, space cooling, potable water, residential-grade natural gas, and liquefied hydrogen as a storable green fuel. The system combines several advanced energy conversion and recovery cycles, including a wind farm, PTSCs, LNG regasification unit, an SRC, an ORC coupled with a TEG unit, a single-effect ARC, a PEME, an RO desalination unit, and a Claude hydrogen liquefaction cycle. The integrated configuration utilizes waste heat recovery and advanced cycle coupling to maximize energy efficiency, exergy utilization, and overall system performance.

Solar thermal energy collection begins with the PTSC field, selected for its high optical efficiency and ability to deliver outlet temperatures exceeding 600 K—sufficient for driving high-performance power cycles. A synthetic heat transfer fluid (HTF), Therminol VP1, circulates through the solar field, absorbing concentrated heat and delivering it to the downstream energy-conversion units (point 1). The high-temperature HTF first supplies heat exchanger 1 (HEX1), which generates superheated steam for the SRC (points 2–3). In the SRC, the pumped water enters the HEX1 and is vaporized (points 5–6), then high-pressure steam expands through the turbine to produce electricity (points 6–7). The exhaust steam exiting the turbine retains substantial thermal energy and is routed to the generator of the single-effect ARC, where a lithium bromide–water solution absorbs the residual heat to produce a cooling load (points 9–18). This arrangement enables efficient utilization of low-grade heat while providing continuous refrigeration output.

The partially cooled HTF leaving the HEX1 still contains usable thermal energy (points 3–4), and is directed to the combined ORC–TEG system (points 19–22). In this configuration, the ORC condenser is replaced by a TEG module (points 21–22), allowing a portion of the remaining heat to be directly converted into electricity via the Seebeck effect. The rejected heat from the ORC–TEG unit is transferred to the LNG stream entering the regasification unit. After the LNG is pumped (points 23–24) and warmed, though it remains at a low temperature (points 24–25), the resulting natural gas expands through a turbine to generate additional power (points 25–26). After expansion, the relatively cold natural gas serves as the initial heat sink for the Claude hydrogen liquefaction cycle (points 26–27), providing the precooling duty required before achieving deep cryogenic temperatures (points 42–43).

Complementing the thermal subsystems, the wind farm contributes intermittent electricity, enhancing system reliability during periods of low solar availability. Freshwater generation is accomplished through an RO desalination unit, which utilizes a portion of the produced electricity to purify seawater, an essential feature for deployment in arid coastal regions (points 28–35). Concurrently, green hydrogen is generated in the PEME using renewable electricity to split water into hydrogen and oxygen (points 36–42). The produced hydrogen is directed to the Claude liquefaction cycle, where it undergoes multistage compression, expansion, and intercooling to reach cryogenic conditions (points 42–57). Liquefaction enables compact, safe, and transportable hydrogen storage, supporting its role as a long-term clean energy carrier within the integrated system. The complete set of thermodynamic properties for all state points labeled in Fig. 1 is provided in Table 10, establishing the baseline for the subsequent analysis.

3. Numerical modeling and simulation methodology

The proposed hybrid wind–solar multi-generation system is modeled using a MATLAB-based simulation platform, which enables flexible implementation of component-level thermodynamic models and system integration [49]. Thermophysical properties of all working fluids are obtained from the NIST REFPROP database, which provides experimentally validated values for temperature, pressure, enthalpy, entropy, and related properties based on internationally recognized equations of state [50]. REFPROP has been extensively benchmarked for a wide range of operating conditions, including near-critical and two-phase regions relevant to power generation and cryogenic processes.

All subsystem models are formulated using fundamental conservation laws of mass, energy, and exergy, together with component-specific correlations adopted from well-established literature. As described in Section 5, the individual models of key components, including the PTSC, PEME, RO unit, ARC, TEG, and hydrogen liquefaction cycle, are independently validated against experimental or high-fidelity numerical data reported in previous studies. The close agreement obtained

Table 1
Input parameters used for system modeling [51–55].

Parameter	Value	Parameter	Value
P_0, (bar)	1.013	**Reverse osmosis desalination unit**	
T_0, (K)	298.15	Pump and turbine conversion efficiency, (%)	85
Solar cycle		Salinity level of the input seawater,(ppm)	35,000
Size of individual collector, (m)	12.27	Salinity concentration of the treated freshwater,(ppm)	450
Pressure reduction, (%)	5	Recovery ratio of the desalination membrane, (−)	0.55
Individual collector width, (m)	5.76	**SRC, ORC, and TEG**	
DNI, (W/m^2)	800	TEG figure of merit, (−)	0.8
Heat loss constant,$(W/m^2.^\circ C)$	3.82	Pinch point temperature of HEX1, (°C)	15
Solar collector area,(m^2)	16,000	Pinch point temperature of HEX2, (°C)	15
Wind farm		Pump and turbine conversion efficiency, (%)	85
Turbine performance factor, (−)	0.9	**PEME**	
Total count of wind turbine units, (−)	5	Cell operating temperature, (K)	353.15
Mean wind velocity, (m/s)	4	Cell Operating pressure, (bar)	1.013
Wind energy capture efficiency, (−)	0.55	Activation energy associated with the anode reaction, (kJ/mol)	76
Rotor span of each turbine, (m)	44	Faraday's constant, (−)	96,485
Single-effect absorption refrigeration cycle		Pre-exponential factor for anode current density, (A/m^2)	1.7×10^5
Evaporator operating temperature, (°C)	5	Relative water content in the cathode electrode, (−)	14
Operating temperature of generator, (°C)	90	Relative water content in the anode electrode, (−)	10
Condenser operating temperature, (°C)	35	Pre-exponential factor for cathode current density, (A/m^2)	4.6×10^3
Absorber operating temperature, (°C)	35	Thickness of the proton exchange membrane,(μm)	100
HEX3 Effectiveness, (−)	0.72	Activation energy for the cathode reaction, (kJ/mol)	18

confirms the capability of the modeling framework to reproduce realistic fluid behavior and system performance over the operating range considered. This integrated numerical framework therefore provides a reliable basis for evaluating energy distribution, system performance, and sources of inefficiency in the proposed configuration. The following boundary conditions and external inputs delineate the problem scope:

- **Primary energy inputs (Source terms):** The system is driven by two renewable fluxes: (i) a solar direct normal irradiance of 800 W/m2 incident on the PTSC field, and (ii) a mean wind velocity of 4 m/s4m/s for the wind farm.
- **Material feed streams:** Inputs include LNG at cryogenic storage conditions, seawater with 35,000 ppm salinity for RO, and high-purity water for PEME.
- **Product delivery boundaries:** Useful outputs including, electricity, cooling, freshwater, regasified natural gas, and liquefied hydrogen are delivered to specified downstream conditions reflecting end-use requirements.
- **System Closure and Reaction Zone:** The control volume is materially closed except for the defined inlets (LNG, seawater, air, PEME feed water) and outlets (products, brine exhaust).

The key input parameters used for the simulations are summarized in Table 1.

3.1. Governing conservation equations

The performance of the proposed hybrid wind–solar multi-generation system is analyzed based on the fundamental conservation principles of mass, energy, and exergy applied under steady-state and steady-flow conditions. The following core assumptions apply to the overall system analysis:

- **Steady-State, Steady-Flow:** All system components operate under steady-state conditions, meaning properties at any point do not change with time.
- **Negligible Kinetic and Potential Energy Changes:** The changes in kinetic and potential energy of the working fluids across components are considered negligible compared to enthalpy changes.
- **Uniform Dead State:** The reference (dead) state for exergy calculations is defined as the ambient condition ($T_0 = 298.15K, P_0 = 101.325\,kPa$).

3.1.1. Mass balance

The mass conservation principle for a general control volume, under the **steady-state assumption**, is formulated as:

$$\sum_{\text{in}} \dot{m}_{\text{in}} - \sum_{out} \dot{m}_{out} = 0 \tag{1}$$

Where, $\dot{m}$ is the mass flow rate, in means input and out means output streams.

3.1.2. Energy balance (First Law of Thermodynamics)

Applying the First Law of Thermodynamics to a control volume under steady-state conditions and neglecting kinetic and potential energy changes, the general energy balance is:

$$\sum_{\text{in}} \dot{m}_{in} h_{in} + \dot{Q} = \sum_{out} \dot{m}_{out} h_{out} + \dot{W} \tag{2}$$

Where, $\dot{Q}$ is the heat transfer rate, $\dot{W}$ is the work output (positive when produced, negative when consumed), and h is the specific enthalpy. For electrical devices (e.g., generators, compressors, PEME), the work term is expressed in terms of electrical power.

3.1.3. Exergy balance (Second Law of Thermodynamics)

Exergy analysis quantifies irreversibilities (exergy destruction) within components. For a control volume at steady-state, the general exergy balance is:

$$\dot{E}x_Q + \sum_{in} \dot{m}_{in} ex_{in} = \dot{E}x_W + \sum_{out} \dot{m}_{out} ex_{out} + \dot{E}x_{dest} \tag{3}$$

The exergy transfer associated with heat and work are:

$$\dot{E}x_Q = \left(1 - \frac{T_0}{T}\right)\dot{Q} \tag{4}$$

$$\dot{E}x_W = \dot{W} \tag{5}$$

The total specific exergy of a stream is the sum of its physical, chemical, kinetic, and potential components:

$$ex = ex^{ph} + ex^{ch} + ex^{kn} + ex^{pt} \tag{6}$$

Consistent with our system-level assumptions, kinetic (ex^{kn}) and potential (ex^{pt}) exergy contributions are neglected, simplifying the expression to:

$$ex \approx ex^{ph} + ex^{ch} \tag{7}$$

The physical exergy component is calculated as:

$$ex^{ph} = h - h_0 - T_0(s - s_0) \tag{8}$$

Where, s is the specific entropy at system conditions, and h_0, s_0 are properties at the dead state (T_0, P_0). Moreover, the chemical exergy of the substances is taken from standard reference values.

Finally, the overall exergy efficiency of the integrated system, defined as the ratio of total useful exergy output to total exergy input, is:

$$\eta_{ex} = \frac{\dot{E}x_{LiquefiedH2} + \dot{W}_{grid} + \dot{E}x_{NG} + \dot{E}x_{freshwater} + \dot{E}x_{cooling}}{\dot{E}x_{wt} + \dot{E}x_{solar} + \dot{E}x_{LNG}} \tag{9}$$

- **Parabolic through solar collectors**

In the suggested system, PTSCs function as the primary source of thermal energy. These collectors are widely utilized due to their high optical efficiency, operational reliability, and ability to achieve fluid outlet temperatures exceeding 600 K, making them well-suited for powering high-performance thermodynamic cycles. The PTSC concentrates incident solar radiation onto a receiver tube located along its focal line. A heat transfer fluid, such as Therminol VP1, circulates through this tube, absorbing the captured solar energy and transporting it to downstream energy conversion components. The thermal performance of a PTSC is influenced by its optical characteristics, convective and radiative heat losses, fluid flow dynamics, and overall heat transfer efficiency. The net rate of usable heat transferred to the working fluid, after accounting for optical absorption and thermal losses, can be expressed as [56,57]:

$$\dot{Q}_u = F_R A_{ap}\left(S_{CL} - \frac{A_{ap}}{A_r}U_L(T_{ri} - T_0)\right) \tag{10}$$

$$A_{ap} = L_{CL}(W - D_{co}) \tag{11}$$

$$\eta_r = \beta\gamma\xi\alpha\kappa \tag{12}$$

$$S_{CL} = G\eta_r \tag{13}$$

$$F_{CL} = \frac{\frac{1}{U_L}}{\frac{1}{U_L} + \frac{D_{ro}}{h_{fi}} + \left(\frac{D_{ro}}{2k}\ln\frac{D_{ro}}{D_{ri}}\right)} \tag{14}$$

$$F_R = \frac{\dot{m}_r C_{P,CL}}{A_r U_L}\left[1 - exp\left(\frac{-A_r U_L F_{CL}}{\dot{m}_r C_{P,CL}}\right)\right] \tag{15}$$

In this analysis, F_R represents the heat removal factor, which measures the effectiveness of transferring the absorbed solar energy to the heat transfer fluid. The parameter U_L is the overall heat loss coefficient, accounting for both convective and radiative losses from the collector to the surroundings. The absorbed solar radiation is expressed as S_{CL}, which quantifies the fraction of incident beam radiation actually captured by the collector surface. Geometric and thermal conditions are also reflected through A_r (receiver area) and A_{ap} (aperture area), while T_{ri} and T_0 correspond to the inlet fluid temperature entering the receiver, and the ambient air temperature, respectively. The term η_r refers to the overall efficiency of the receiver in capturing and transferring absorbed solar radiation.

- **Wind turbine**

To complement solar energy, the system integrates a wind farm, which enhances electricity reliability and mitigates the effects of solar intermittency. Each wind turbine converts the kinetic energy of moving air into electrical power through a combination of aerodynamic capture, mechanical rotation, and generator conversion. The extractable power depends mainly on the air density, the rotor's swept area, the cube of the wind speed, and the rotor's aerodynamic performance, quantified by the power coefficient. The electrical power output of a wind turbine is expressed as [51]:

$$\dot{W}_{wt} = \frac{1}{2}\eta_{wt}\rho_{air}A_{wt}C_{P,wt}(V_{wind})^3 \tag{16}$$

In this formulation, η_{wt} is the turbine efficiency, ρ_{air} is air density, A_{wt} is rotor area, $C_{P,wt}$ is the power coefficient, and V_{wind} is wind speed. The aerodynamic power before conversion is [51]:

$$\dot{W}_{wt,i} = \frac{1}{2}\rho_{air}A_{wt}C_{P,wt}(V_{wind})^3 \tag{17}$$

The wind exergy and exergy losses are [51]:

$$\dot{E}x_{wt} = \frac{1}{2}\rho_{air}A_{wt}(V_{wind})^3 \tag{18}$$

$$\dot{E}x_{des,wt} = \left(\frac{1}{C_{P,wt}}\right)\dot{W}_{wt} \tag{19}$$

Table 2
LNG regasification cycle equations [58].

Component	Equation
LNG pump	$\dot{W}_{Pump,LNG} = \dot{m}_{LNG}(h_{24} - h_{23})$
LNG evaporator	$\dot{Q}_{Eva,LNG} = \dot{m}_{LNG}(h_{25} - h_{24})$
Cooling load generator	$\dot{Q}_{Cooling,LNG} = \dot{m}_{LNG}(h_{27} - h_{26})$
LNG turbine	$\dot{W}_{Tur,LNG} = \dot{m}_{LNG}(h_{25} - h_{26})$

- **LNG regasification unit**

In the proposed system, an LNG regasification unit is incorporated to harness low-grade waste heat and supply the cryogenic energy needed for hydrogen liquefaction. The process begins with LNG being pumped from the storage tank to the evaporator, which is thermally coupled with the TEG integrated with the ORC. At this stage, heat rejected from the TEG is recovered to vaporize the LNG, effectively utilizing energy that would otherwise be lost. The vaporized natural gas is then expanded through an LNG turbine, producing mechanical power that supplements the system's total electricity output. After expansion, the cold exhaust from the LNG turbine is directed to a cooling stage, where its cryogenic potential is exploited to provide the necessary low-temperature input for the Claude hydrogen liquefaction cycle. In the present model, LNG is utilized both as a heat recovery medium and as a cryogenic source for hydrogen liquefaction [58]. The main governing relationships for the LNG regasification process are summarized in Table 2.

- **Steam and organic Rankine cycles**

The hybrid system integrates both an SRC and an ORC to efficiently convert thermal energy into electricity over a wide temperature range. In the SRC, high-pressure, high-temperature steam generated from the solar field carries significant thermal energy, which is converted into mechanical work as it expands through the turbine, taking advantage of the high enthalpy difference between the outlet and inlet. The ORC, on the other hand, employs an organic working fluid with a low boiling point, enabling the recovery of low- to medium-grade heat that would be otherwise wasted in conventional cycles. By selecting a suitable organic fluid, the ORC can efficiently exploit residual heat from the SRC or other low-temperature sources, increasing the overall energy utilization of the system. Together, these cycles complement each other: the SRC extracts maximum energy from high-temperature heat, while the ORC captures additional energy from lower-temperature streams, thereby improving total electrical output and enhancing exergy efficiency. The generated power by the turbines is determined by the enthalpy difference across the turbine:

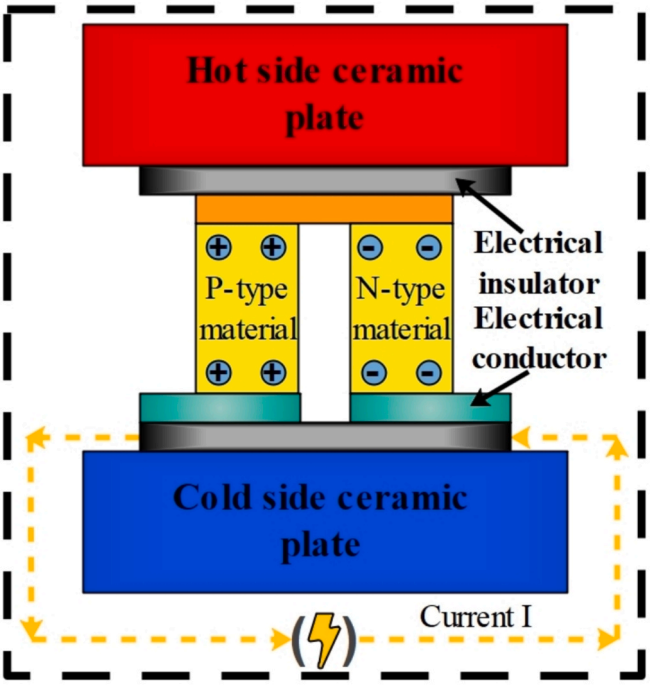

Fig. 2. Schematic diagram of a TEG unit.

$$\dot{W}_{turbine} = \dot{m}\left(h_{in,turbine} - h_{out,turbine}\right) \tag{20}$$

Where $h_{in,turbine}$ and $h_{out,turbine}$ are the turbine inlet and outlet enthalpies, and $\dot{m}$ is the working fluid mass flow rate. The heat input to each cycle is given by:

$$\dot{Q}_{in,Rankinecycle} = \dot{m}\left(h_{in,Rankinecycle} - h_{feed}\right) \tag{21}$$

The thermal efficiency of the cycles is expressed as the ratio of net turbine work to heat input:

$$\eta_{Rankinecycle} = \frac{\dot{W}_{turbine}}{\dot{Q}_{in,Rankinecycle}} \tag{22}$$

By combining SRC and ORC, the system efficiently exploits both high- and low-temperature heat sources, maximizing electrical output and enhancing overall exergy utilization.

- **Thermoelectric generator unit**

The TEG unit in the hybrid system is employed to convert low- to medium-grade thermal energy directly into electricity through the Seebeck effect, enhancing overall system efficiency by utilizing residual heat [59,60]. The performance of TEGs is fundamentally governed by thermodynamic principles that relate temperature differences across the device to the generated voltage and efficiency. The TEG unit is depicted in Fig. 2.

The efficiency of a TEG can be expressed as [51,61]:

$$\eta_{TEG} = \eta_{carnot}\frac{\sqrt{1+ZT_{av}} - 1}{\sqrt{1+ZT_{av}} + \frac{T_L}{T_H}} \tag{23}$$

$$\eta_{carnot} = 1 - \frac{T_L}{T_H} \tag{24}$$

$$ZT_m = \frac{\alpha^2 T_{av}}{\sigma R} \tag{25}$$

$$T_{av} = \frac{T_L + T_H}{2} \tag{26}$$

$$\alpha = -\frac{\Delta V}{\Delta T} \tag{27}$$

In this formulation, T_H and T_L represent the temperatures at the hot and cold sides of the thermoelectric module, respectively, while T_{av} denotes the average operating temperature across the device. The Seebeck coefficient, α, characterizes the voltage generated per unit temperature difference, σ represents the thermal conductivity of the module material, and R is the internal electrical resistance. The dimensionless figure of merit, ZT_m, combines these properties and plays a critical role in determining the thermoelectric conversion efficiency. The theoretical electrical power output of the TEG, which is based on the energy transferred from the working fluid and the heat source, is calculated as [51,61]:

$$\dot{W}_{TEG} = \dot{m}_{21}(h_{21} - h_{22}) - \dot{m}_{26}(h_{27} - h_{26}) \tag{28}$$

In this system, the TEG is thermally coupled to the ORC condenser, allowing it to recover the low-grade heat rejected by the ORC working fluid, thereby producing additional electricity and improving the overall exergy utilization of the multi-generation system.

- **Single-effect LiBr absorption refrigeration cycle**

In the proposed hybrid system, low-temperature cooling is provided by a single-effect ARC using a lithium bromide–water solution, which efficiently converts waste heat from the steam Rankine cycle into useful cooling. Unlike conventional electrically driven vapor-compression systems, this cycle relies entirely on thermal energy to drive the refrigeration process. In the ARC, the lithium bromide solution absorbs water vapor in the absorber, forming a concentrated solution that is subsequently heated in the generator to release the refrigerant as vapor. This vapor is condensed, expanded, and then evaporated to produce the cooling effect. The cycle's cooling capacity is determined by the mass flow rate of the refrigerant and its enthalpy difference across the evaporator:

$$\dot{Q}_{Cooling} = \dot{Q}_{evap} = \dot{m}_{ref}\left(h_{out,evap} - h_{in,evap}\right) \tag{29}$$

- **Reverse osmosis desalination unit**

The RO desalination unit is incorporated into the hybrid system to produce freshwater from seawater using electrical energy generated by the system. RO is a membrane-based separation process in which pressurized feedwater is forced through a semipermeable membrane, allowing water molecules to pass while retaining dissolved salts and impurities. The permeate flow rate is determined by the applied pressure, membrane properties, and the osmotic pressure of the feedwater. The volumetric flow rate of freshwater produced can be expressed as [52,62]:

$$\dot{V}_p = A_m L_P(\Delta P - \Delta\pi) \tag{30}$$

where A_m is the membrane area, L_P is the membrane permeability, ΔP is the applied hydraulic pressure, and $\Delta\pi$ is the osmotic pressure difference across the membrane. The required pump power to drive the RO process is given by [52,62]:

$$\dot{W}_{pump} = \frac{\dot{V}_f \Delta P}{\eta_{pump}} \tag{31}$$

where $\dot{V}_f$ is the feedwater flow rate and η_{pump} is the pump efficiency. The recovery ratio, representing the fraction of feedwater converted into permeate, is defined as [52,62]:

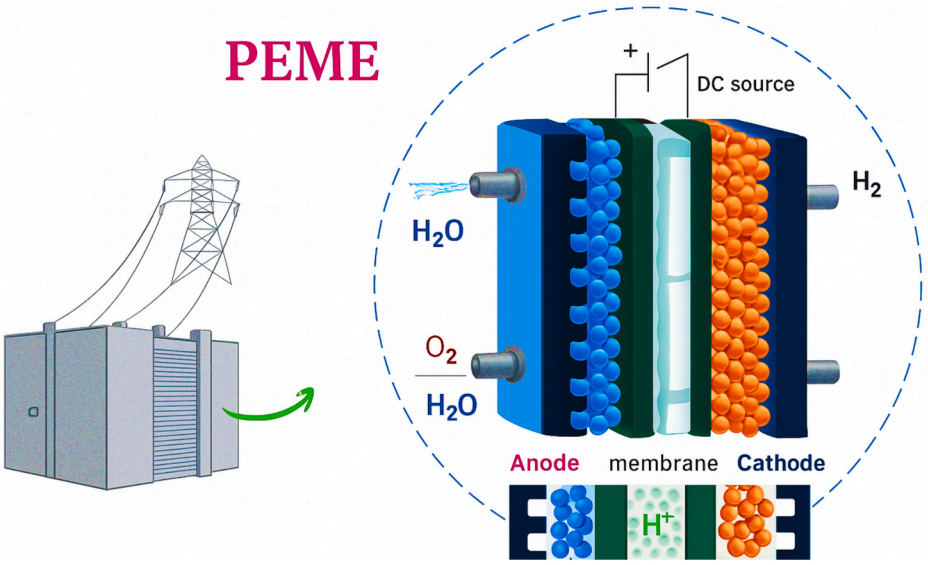

Fig. 3. Schematic diagram of one cell of a PEME.

$$R_r = \frac{\dot{V}_p}{\dot{V}_f} \tag{32}$$

RO desalination is energy-intensive compared to thermal desalination methods; however, when integrated with renewable electricity sources, such as the wind–solar hybrid system, it becomes a sustainable solution for addressing water scarcity.

- **Hydrogen generation subsystem**

Hydrogen is generated in the proposed multi-generation system using a PEME, which splits water into hydrogen and oxygen by utilizing electricity supplied from the hybrid wind–solar power system. The PEME is widely preferred because of its high current density, compact structure, and fast dynamic response to the intermittent nature of renewable energy sources. Fig. 3 shows the schematic diagram of one cell of PEME.

The electrochemical process begins when electrical energy drives the water-splitting reaction, with the required input energy expressed as [52–54]:

$$E_{elec} = Q_{elec} = JV \tag{33}$$

where J is the current density and V is the cell voltage. The thermodynamic energy requirement for water electrolysis is described by the enthalpy relation [52–54]:

$$\Delta H = \Delta G + T\Delta S \tag{34}$$

where ΔG is the Gibbs free energy and $T\Delta S$ represents the entropy contribution. The reversible cell potential is determined by the Nernst equation [52–54]:

$$V = V_0 + V_{ohm} + V_{activ,a} + V_{activ,c} \tag{35}$$

$$V_0 = 1.229 - 8.5 \times 10^{-4}(T_{PEM} - 298) \tag{36}$$

$$V_{activ,i} = \frac{RT}{F} sinh^{-1}\left(\frac{J}{2J_{0,i}}\right), i = a, c \tag{37}$$

$$V_{ohm} = JR_{PEM}, R_{PEM} = \int_0^D \frac{dx}{\sigma[\lambda(x)]} \tag{38}$$

In practice, the actual cell voltage is higher than the reversible potential due to overpotentials. Here, V_{ohm} denotes the ohmic losses, while $V_{activ,a}$ and $V_{activ,c}$ correspond to the activation overpotentials at the anode and cathode, respectively. The ohmic resistance depends on ionic transport through the membrane, with D representing the membrane thickness and $\sigma[\lambda(x)]$ the local ionic conductivity. The exchange current density at each electrode, which defines the activation overpotential, is given as [52–54]:

$$J_{0,i} = J_i^{ref} exp\left(-\frac{E_{activ,i}}{RT}\right) i = a, c \tag{39}$$

The distribution of water content across the membrane, $\lambda(x)$, can be approximated linearly as [52]:

$$\lambda(x) = \lambda_c + \frac{\lambda_a - \lambda_c}{D} x \tag{40}$$

Where λ_a and λ_c represent the water content at the anode and cathode sides, respectively. The corresponding local ionic conductivity is expressed as [52–54]:

$$\sigma[\lambda(x)] = (0.5139\lambda(x) - 0.326) \times \exp\left(1268\left(\frac{1}{303} - \frac{1}{T}\right)\right) \tag{41}$$

These relations provide a rigorous framework for evaluating the energy requirements, polarization losses, and overall hydrogen production efficiency of the PEME. When integrated with renewable electricity, the PEME enables sustainable and carbon-free hydrogen generation, which can then be utilized in the hydrogen liquefaction cycle for storage and transportation.

- **Hydrogen liquefication unit**

Hydrogen storage and transportation in its gaseous form pose significant technical and economic challenges due to its low density and high pressurization requirements. To overcome these limitations, the present system incorporates a Claude liquefaction cycle to convert hydrogen into its liquid state, thereby enabling compact, safe, and long-term storage. The Claude process involves multiple stages, beginning with the compression of hydrogen to pressures typically between 2 and 13 MPa, followed by staged cooling through heat exchangers to progressively reduce its temperature. The precooled hydrogen stream then undergoes expansion through a throttling valve, where it enters a two-phase region and partially liquefies. The liquid fraction is collected in

Table 3
Governing equations for Claude hydrogen liquefaction cycle modeling [64,65].

Component	Equations
Compressor	$\dot{m}_{44} = \dot{m}_{45}\dot{W}_{comp,act} = \frac{\dot{m}_{44}RT_0 ln(P_{45}/P_{44})}{\eta_{comp}}\dot{W}_{comp,rev} = \dot{m}_{39}(ex_{45} - ex_{44})\eta_{comp} = \frac{h_{45,s} - h_{44}}{h_{45} - h_{44}}\varepsilon_{comp} = \frac{\dot{W}_{comp,rev}}{\dot{W}_{comp,act}}$
HEX 4	$\dot{m}_{45} = \dot{m}_{46}; \dot{m}_{56} = \dot{m}_{57} = \dot{m} = \dot{m}_{52}\dot{m}_{45}(h_{45} - h_{46}) = \dot{m}_{56}(h_{57} - h_{56})\varepsilon_{HEX4} = \frac{\dot{m}_{56}(ex_{57} - ex_{56})}{\dot{m}_{45}(ex_{45} - ex_{46})}$
Expander	$\dot{m}_{47'} = \dot{m}_{47''}\dot{W}_{expa,act} = \dot{m}_{47'}(h_{47'} - h_{47''}); \eta_{expa} = \frac{h_{47'} - h_{47''}}{h_{47',s} - h_{47''}}\dot{W}_{expa,rev} = \dot{m}_{47'}(ex_{47'} - ex_{47''}); \varepsilon_{expa} = \frac{\dot{W}_{expa,act}}{\dot{W}_{expa,rev}}$
HEX 5	$\dot{m}_{48} = \dot{m}_{49}; \dot{m}_{55} = \dot{m}_{56}\dot{m}_{48}(h_{48} - h_{49}) = \dot{m}_{55}(h_{56} - h_{55})\varepsilon_{HEX5} = \frac{\dot{m}_{55}(ex_{56} - ex_{55})}{\dot{m}_{48}(ex_{48} - ex_{49})}$
HEX 6	$\dot{m}_{49} = \dot{m}_{50}; \dot{m}_{54} = \dot{m}_{53}; \dot{m}_{53} = \dot{m} - \dot{m}_{47''} - \dot{m}_{52}\dot{m}_{49}(h_{49} - h_{50}) = \dot{m}_{53}(h_{54} - h_{53})\varepsilon_{HEX6} = \frac{\dot{m}_{53}(ex_{54} - ex_{53})}{\dot{m}_{49}(ex_{49} - ex_{50})}$
J-T Valve	$\dot{m}_{50} = \dot{m}_{51}; h_{50} = h_{51}\varepsilon_{J-T} = \frac{\dot{m}_{51}ex_{51}}{\dot{m}_{50}ex_{50}}$
Receiver	$\dot{m}_{53} = \dot{m} - \dot{m}_{47''} - \dot{m}_{52}\dot{m}_{52}h_{52} + \dot{m}_{53}h_{53} = \dot{m}_{51}h_{51}\varepsilon_{rec} = \frac{\dot{m}_{53}ex_{53} + \dot{m}_{52}ex_{52}}{\dot{m}_{51}ex_{51}}$

a cryogenic storage tank, while the unliquefied gaseous fraction is recirculated into the cycle for further processing, thereby improving efficiency [63]. The main governing equations for modeling the Claude liquefaction cycle are listed in Table 3.

3.2. Economic analysis

Evaluating the economic performance of a hybrid wind–solar multi-generation system is essential for determining its feasibility, cost-effectiveness, and long-term sustainability. This analysis considers both the initial capital investment and ongoing operational and maintenance expenses, allowing informed decisions on system design and optimization. To annualize the capital expenditure over the project lifetime, the capital recovery factor (CRF) is employed [66,67]:

$$CRF = \frac{i(1+i)^N}{(1+i)^N - 1} \tag{42}$$

where i is the annual interest rate and N is the equipment lifetime in years. For this study, standard assumptions of a 12% interest rate and a 20-year lifespan are adopted, reflecting typical renewable energy project conditions. The total annualized system cost is then calculated by summing the annualized costs of all components, while accounting for maintenance through a correction factor φ, and dividing by the total operating hours per year (t_{hour}), assumed to be 8,000 h for near-continuous operation [66,67]:

$$\dot{Z}_{tot} = \frac{CRF \times \varphi \times \sum Z_k}{t_{hour}} \tag{43}$$

Here, $\varphi = 1.06$ accounts for a 6% increase in costs due to routine servicing and repairs. This approach enables a systematic comparison of capital and operating expenses across the system, ensuring economically optimal design choices. Mathematical equations used to quantify the capital and operational costs of each system component are listed in Table 4. Furthermore, the levelized cost of hydrogen (LCOH) is defined as the ratio of the total system cost rate to the corresponding hydrogen production rate and is expressed as:

$$LCOH(\$/kg) = \frac{\dot{Z}_{tot}(\$/h)}{\dot{m}_{Liquid-H2}(kg/h)} \tag{44}$$

3.3. Environmental analysis

The environmental dimension of energy system evaluation is of paramount importance, especially within the framework of worldwide

Table 4
Mathematical equations used to quantify the capital and operational costs of each system component [51,55,68,69].

Subsystem	Cost functions
PTSCs	$Z_{PTSC} = 240 \times A_{ap,tot}$
HEXs	$Z_{HX1} = 2143 \times (A_{HX1})^{0.514}$
Pump	$Z_{pump} = 200 \times \left(\dot{W}_{pump}\right)^{0.65}$
Turbine	$Z_{tur} = 479.34 \times \left(\frac{\dot{m}}{0.92 - \eta_{tur}}\right) \times \log(R_{P,tur}) \times (1 + \exp(0.36 \times T_8 - 54.4)$
Compressor	$Z_{Comp} = 71.1 \times \left(\frac{\dot{m}}{1 - \eta_{Comp}}\right) \times \log(R_{P,comp}) \times R_{P,comp}$
Regenerator	$Z_{Reg} = 2143 \times (A_{Reg})^{0.514}$
Heater	$Z_{Pre} = 130 \times (\frac{A_{Pre}}{0.093})^{0.78}$
PEME	$Z_{PEME} = 1000 \times \dot{W}_{elec}$
Wind turbine	$Z_{WT} = 3465 \times (\dot{W}_{wt})^{0.5366}$
Absorber	$Z_{Abs} = 16000 \times (A_{Abs}/100)^{0.6}$
RO HPP	$\log_{10}(Z_{RO,P}) = 3.3892 + 0.0536\log_{10}\left(\dot{W}_{RO,P}\right) + 0.1538\left[\log_{10}\left(\dot{W}_{RO,P}\right)\right]$
RO module	$Z_{RO} = 10N.A_m$
Pelton Turbine	$\log_{10}(Z_{PT}) = 2.2476 + 1.4965\log_{10}\left(\dot{W}_{PT}\right) - 0.1618\left[\log_{10}\left(\dot{W}_{PT}\right)\right]^2$
SWIPS	$Z_{SWIPS} = 996\dot{Q}_f$
Inter cooler	$Z_{int} = 1773\dot{m}$
Evaporator	$Z_{Evap} = 309.14(A_{Evap})^{0.85}$
Condenser	$Z_{Cond} = 516.62(A_{Cond})^{0.6}$
Claude compressor	$Z_{Comp2} = 71.1 \times \left(\frac{\dot{m} \times R_{P,comp2}}{0.01}\right) \times \ln(R_{P,comp2})$
Claude HEXs	$Z_{ClaudeHEXs} = 2143 \times (A_{HEXs})^{0.514}$
J-T valve	$Z_{J-T} = 114.5(\dot{m} - \dot{m}_e)$
Separator	$Z_{Sep} = 280.3(\dot{m} - \dot{m}_e)^{0.67}$
Expander	$Z_{WT} = 4750 \times (\dot{W}_{Exp})^{0.514}$

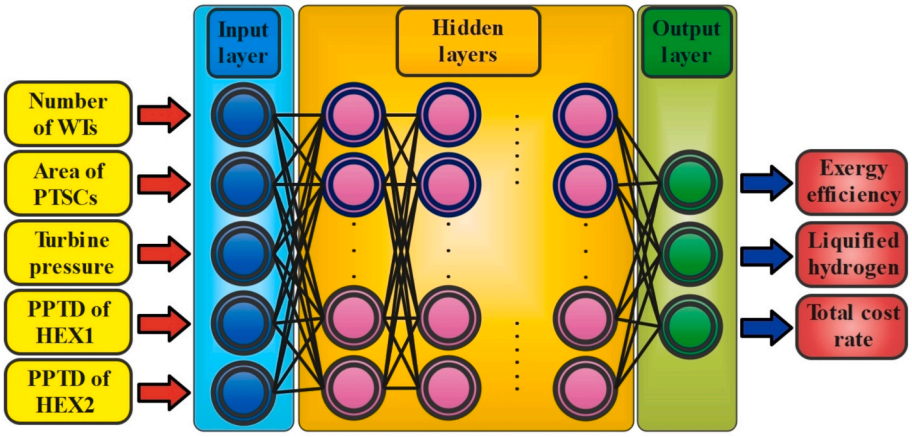

Fig. 4. Schematic diagram of the ANN architecture.

initiatives aimed at combating climate change and minimizing environmental degradation. Unlike fossil fuel-based technologies, hybrid wind–solar systems operate without direct combustion, thereby eliminating emissions of greenhouse gases, nitrogen oxides, sulfur oxides, and particulate matter. This transition not only lowers the carbon footprint but also alleviates associated public health risks and reduces stress on freshwater resources that are often consumed in thermal power plants. Additionally, by harnessing renewable sources, the system decreases dependency on finite natural gas reserves and promotes long-term energy security.

The environmental performance of the multi-generation system is quantified determining the extent to which it decreases carbon dioxide emissions in comparison with a conventional natural gas-fired power facility. The reduction in CO_2 emissions per unit of electricity generated is calculated as:

$$\Delta \dot{m}_{CO_2} = \dot{W}_{net} \times e_{CO_2} \tag{45}$$

Here, e_{CO_2} denotes the emission factor for natural gas, taken as 0.18 kg of CO_2 per kilowatt-hour. Furthermore, the economic benefits of reducing CO_2 emissions are evaluated through the emission reduction cost (ERC), defined as:

where $\dot{W}_{net}$ is the net electrical output of the system, and e_{CO_2} is the emission factor of natural gas, taken as 0.18 kg CO_2/kWh. Beyond the environmental benefits, the financial implications of emission reductions are assessed through the emission reduction cost (ERC), which accounts for the monetary value of avoided carbon emissions:

$$ERC_{CO_2} = \Delta \dot{m}_{CO_2} \times C_{CO_2} \tag{46}$$

Here, C_{CO_2} represents the cost of CO_2 emissions, valued at 0.024 USD/kg. This dual assessment highlights not only the contribution of the hybrid system to climate change mitigation but also its potential to generate economic savings through reduced carbon liabilities. Consequently, the integration of solar and wind energy into the proposed design demonstrates a strong alignment with sustainable development goals by combining ecological responsibility with financial viability.

4. Ann-based optimization

Optimizing complex hybrid renewable multi-generation systems requires handling multiple, interdependent objectives, such as maximizing exergy efficiency and hydrogen output while minimizing system costs. In this work, an ANN is implemented as a surrogate model to emulate the nonlinear behavior of the proposed wind–solar poly-generation system. The ANN is trained using datasets generated from thermodynamic and economic simulations, allowing rapid evaluation of system responses with minimal computational demand compared to conventional simulation-based optimization approaches.

Table 5
Input parameters and hyperparameters employed in ANN training.

Parameter	Value
Generated data	1000
Data generation method	Random
Validation data	15%
Training data	70%
Test data	15%
Maximum epoch	1000
Number of hidden layers	6
Neurons in each layer	10

Table 6
Range of variation for the objective functions and decision variables.

Parameter	Lower bound	Upper bound
Decision variables		
Number of wind turbines (−)	1	10
Total area of PTSCs (m^2)	10,000	20,000
Turbine inlet pressure,(kPa)	1000	3500
Pinch point temperature differences of HEX1 ($^\circ$C)	10	35
Pinch point temperature differences of HEX2 ($^\circ$C)	10	35
Objective functions		
Exergy efficiency ($\eta_{ex,tot}$)	Should be maximized	
Liquefied hydrogen production rate (kg/h)	Should be maximized	
Total cost rate ($\dot{Z}_{tot}$)	Should be minimized	

The developed ANN consists of an input layer, an output layer, and six hidden layers. The selected input parameters include the number of wind turbines, the total aperture area of PTSCs, the turbine inlet pressure, and the pinch point temperature differences of heat exchangers HEX1 and HEX2. The outputs of interest are defined as the liquefied hydrogen production rate, the overall exergy efficiency, and the total cost rate. The network is trained using the Levenberg–Marquardt backpropagation algorithm, chosen for its superior convergence performance in nonlinear optimization problems. To ensure robustness, the dataset is divided into training, validation, and testing subsets. Fig. 4 shows the architecture of the ANN used in this study. Table 5 summarizes the input variables and hyperparameters employed in the ANN training process.

The decision variables and their variation ranges are summarized in Table 6. These parameters represent the adjustable design and operating conditions of the system, while the optimization objectives are to maximize liquified hydrogen production rate and exergy efficiency and to minimize the total cost rate.

Table 7
Parameters used in NSGA-II optimization method.

Parameter	Method/Value
Maximum generation	100
Number of variables	5
Crossover fraction	0.8
Population size	200
Function	1e-4
Selection method	Tournament

After training, the ANN is integrated with the NSGA-II to perform multi-objective optimization. NSGA-II is a widely used evolutionary algorithm that effectively investigates trade-offs among competing objectives and produces a Pareto-optimal front. In this study, it is utilized to determine optimal system configurations that enhance exergy efficiency and liquefied hydrogen production while reducing the total cost rate. The use of ANN within the optimization framework accelerates the search process, as system evaluations are carried out through fast ANN predictions instead of computationally expensive simulations. The Pareto frontier diagrams generated by NSGA-II provide valuable insights into the trade-offs between energy, environmental, and economic performance indicators. The parameters employed in the NSGA-II optimization are summarized in Table 7.

5. System verification

Given the novelty of the proposed hybrid poly-generation system, no comprehensive experimental benchmark exists for the entire integrated configuration. Consequently, the reliability of the system model is established by independently validating each major subsystem against well-documented experimental or numerical results from the literature.

For the solar thermal unit, the simulated heat transfer performance is compared with the experimental results reported by Al-Suliman et al. [70], as illustrated in Fig. 5(a). The comparison demonstrates close agreement, with deviations falling within acceptable engineering limits. Similarly, the PEME is validated using experimental data from Ref. [71], as shown in Fig. 5(b). The results confirm excellent consistency, with a maximum deviation of less than 1%, confirming the accuracy of the PEME modeling approach.

The RO desalination subsystem is verified by comparing model predictions with data reported Sharqawy et al. [72], presented in Fig. 5 (c). The outcomes show strong alignment, indicating that the developed RO model can reliably capture water production performance. Finally, the TEG is validated against the results of Ziapour et al. [73], in which power output was analyzed as a function of the TEG figure of merit (ZT_m). As shown in Fig. 5(d), the modeled TEG response closely matches the reported data, further confirming its accuracy. Overall, these comparisons collectively demonstrate that the developed system components are robust and reliable, providing confidence in the validity of the integrated system model.

The single-effect ARC model was verified using the results of

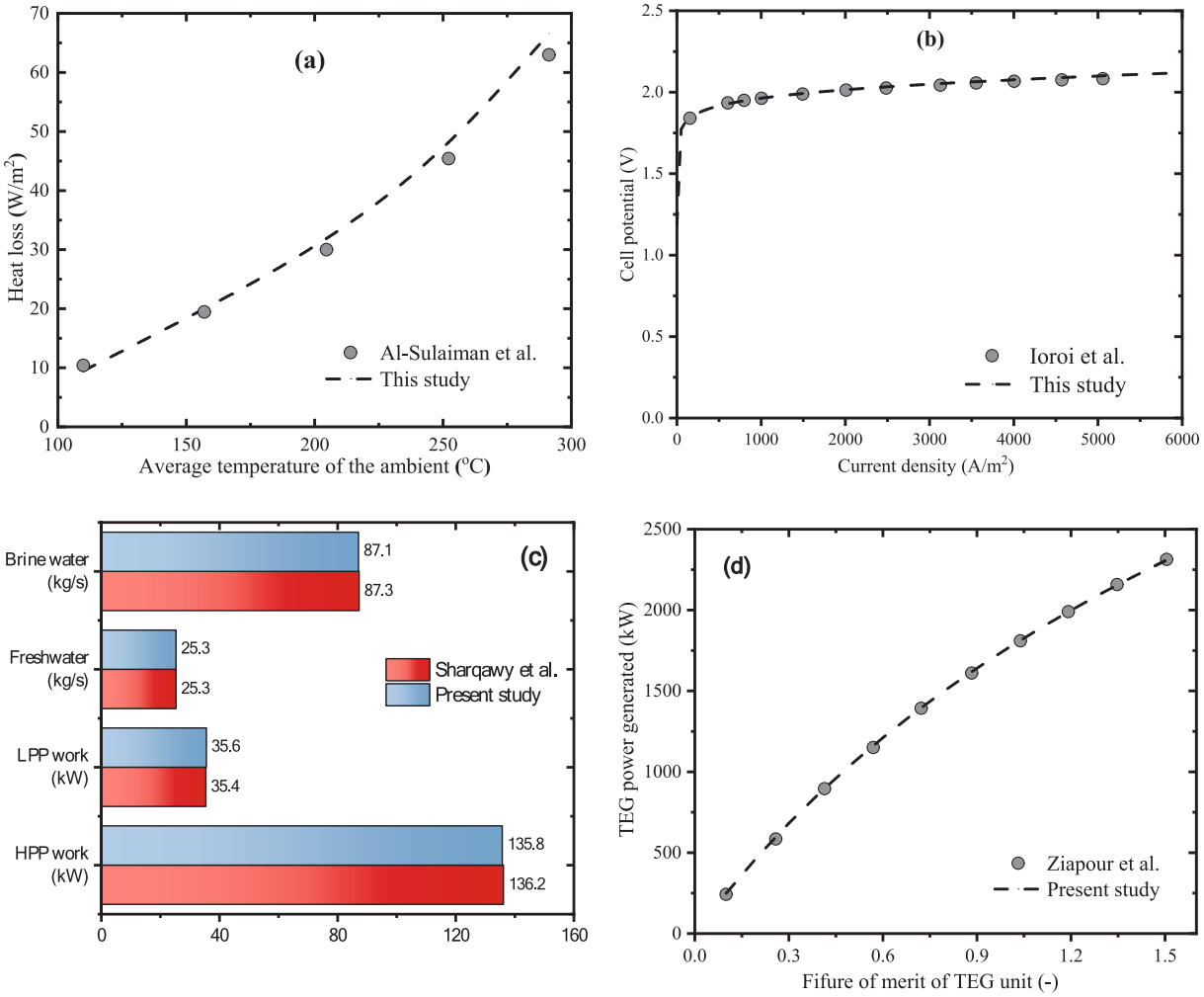

Fig. 5. Subsystem model verification: (a) PTSCs with Ref. [70], (b) PEME with Ref. [71], (c) RO unit with Ref. [72], and (d) TEG unit with Ref. [73].

Table 8
Performance comparison of the developed single-effect ARC model with Maryami et al. [74].

Parameter	Maryami et al. [74]	Present study
$Coolingloadinevaporator(kW)$	300	320.46
Mass flow ratio of solution to refrigerant (−)	6.22	6.19
$Aborbedheatbyabsorber(kW)$	352.3	366.4
COP(−)	0.825	0.829

Table 9
Baseline system performance.

Parameter	Value
$\dot{W}_{SRC}(kW)$	666.77
$\dot{W}_{SRC}(kW)$	666.77
$\dot{W}_{ORC}(kW)$	228.59
$\dot{W}_{TEG}(kW)$	70.69
$\dot{W}_{Grid}(kW)$	937.13
$\dot{Q}_{Cooling}(kW)$	2295.8
$\dot{m}_{freshwater}(kg/s)$	14.86
$\dot{m}_{Liquid-H2}(kg/h)$	3.21
$LCOH(\$/kg)$	3.53
$\dot{E}x_{D,total}(MW)$	9.91
$\eta_{ex}(\%)$	12.11
$\dot{Z}_{tot}(\$/h)$	162.69
$ERC_{CO_2}(\$/h)$	7.75

Maryami et al. [74]. As shown in Table 8, the output cooling load in evaporator, absorber heat duty, mass flow ratio, and *COP* closely match the reference data, with only minor deviations. These results confirm the accuracy and reliability of the developed single-effect ARC model.

6. Results and discussion

This section details the performance assessment of the proposed hybrid wind–solar poly-generation system through a comprehensive fourfold evaluation encompassing energy, exergy, economic, and environmental metrics. Initially, the system is examined under baseline operational conditions to establish reference performance indicators. Subsequently, a parametric study explores how variations in critical design and operational parameters influence energy output, hydrogen production, and overall efficiency. Following this, a surrogate-assisted multi-objective optimization using ANN and NSGA-II is applied to uncover optimal configurations that balance exergy efficiency, liquefied hydrogen yield, and total system cost. Finally, a practical case study simulates system operation using real meteorological and energy demand data to demonstrate the feasibility, reliability, and applicability of the integrated poly-generation concept in real-world scenarios.

6.1. Baseline system

The baseline analysis offers insight into the functional performance of the proposed hybrid wind–solar poly-generation system under standard operating conditions. Key performance metrics are summarized in Table 9. A designated fraction of the generated electricity, 10% sourced from the wind farm and the combined SRC and ORC-TEG cycles, is allocated to the reverse osmosis unit, ensuring a continuous supply of desalinated water. Similarly, 10% of the total power is utilized by the PEM electrolyzer to enable green hydrogen production. Under these baseline conditions, the system produces 937.13 kW of usable electricity suitable for grid integration, 2295.8 kW of cooling via the absorption refrigeration cycle, 14.86 kg/h of fresh water, and 3.21 kg/h of liquefied hydrogen. Thermodynamic assessment indicates an overall exergy efficiency of 12.11%, while the economic analysis yields a levelized cost of hydrogen (LCOH) of 3.53 $/kg and a total operational cost of 162.69 $/h. These findings highlight the system's capability to deliver multiple energy services effectively, achieving a balance between operational efficiency and economically competitive hydrogen production. Thermodynamic characteristics of each streamline for the baseline system configuration is presented in Table 10.

Table 10
Thermodynamic state points for the baseline system configuration.

State Point	Fluid	T (K)	P (bar)	h (kJ/kg)	s ($kj/kg.K$)
1	Therminol VP-1	373.17	11.51	126.43	0.37
2	Therminol VP-1	604.43	11.01	609.66	1.37
3	Therminol VP-1	463.15	10.51	297.33	0.78
4	Therminol VP-1	373.15	10.01	126.24	0.37
5	Water	303.15	1.013	125.82	0.44
6	Water	303.21	15.99	127.41	0.44
7	Water	589.43	15.19	3073.8	6.98
8	Water	374.49	1.06	2594.98	7.12
9	LiBr-water	308.2	0.0088	85.02	0.2117
10	LiBr-water	308.2	0.056	85.02	0.2117
11	LiBr-water	336.6	0.056	143	0.3919
12	LiBr-water	351.2	0.056	187.9	0.4456
13	LiBr-water	318.9	0.056	125.5	0.2591
14	LiBr-water	318.9	0.056	125.5	0.2591
15	Water	351.2	0.056	2646	8.601
16	Water	308.2	0.056	146.6	0.505
17	Water	308	0.056	146.6	0.505
18	Water	278.2	0.056	2510 258.99	9.024
19	Isobutane	298.83	13.4379	261.2	1.2
20	Isobutane	448.15	12.766	883.68	2.94
21	Isobutane	415.02	3.85	821.39	2.95
22	Isobutane	298.15	3.67	258.99	1.21
23	Natural gas	111.45	1.013	− 911.7	− 6.684
24	Natural gas	111.98	15	− 907.81	− 6.674
25	Natural gas	231.95	15	− 166.78	− 2.009
26	Natural gas	163.72	3	− 294.35	− 1.867
27	Natural gas	283	3	− 36.68	− 0.686
28	Saline water	298.15	1.013	99.7	0.35
29	Saline water	298.15	6.58	100	0.35
30	Saline water	298.15	6.32	100	0.35
31	Saline water	298.15	6.07	100	0.35
32	Saline water	298.15	72.8	107	0.35
33	Fresh water	298.15	1.013	105	0.37
34	Brine water	298.15	51.0	94.6	0.29
35	Brine water	298.15	1.013	89.1	0.29
36	Water	298.15	1.013	104.92	0.367
37	Water	353.15	1.013	335.05	1.075
38	Water	353.15	1.013	335.05	1.075
39	Water	353.15	1.013	335.05	1.075
	Oxygen			321.84	6.56
40	Water	353.15	1.013	335.05	1.075
41	Oxygen	353.15	1.013	321.84	6.56
42	Hydrogen	353.15	1.013	4720.6	55.805
43	Hydrogen	231.7	1.013	2992.5	49.81
44	Hydrogen	222.5	1.013	2864.9	49.25
45	Hydrogen	222.5	50	2873.5	33.07
46	Hydrogen	172.6	50	2184.5	29.57
47	Hydrogen	160.15	50	2017.4	28.56
47′	Hydrogen	160.15	50	2017.4	28.56
47″	Hydrogen	63.15	1.013	906.56	34.25
48	Hydrogen	160.15	50	2017.4	28.56
49	Hydrogen	59.5	50	686.66	15.32
50	Hydrogen	47.3	50	453.76	10.91
51	Hydrogen	20.56	1.013	451.01	22.14
52	Hydrogen	20.56	1.013	451.01	22.14
53	Hydrogen	20.56	1.013	451.01	22.14
54	Hydrogen	65.15	1.013	927.58	34.58
55	Hydrogen	74.7	1.013	1028.5	36.028
56	Hydrogen	135.8	1.013	1725.6	42.798
57	Hydrogen	210.3	1.013	2697.3	48.48

Fig. 6 presents the sensitivity analysis of the proposed hybrid system, revealing that system performance is most strongly influenced by the number of wind turbines and the area of the PTSC field, as indicated by their dominant impacts across all objective functions. The number of wind turbines exhibits the highest sensitivity on exergy efficiency (76.05%), total cost rate (13.77%), grid power interaction (63.12%),

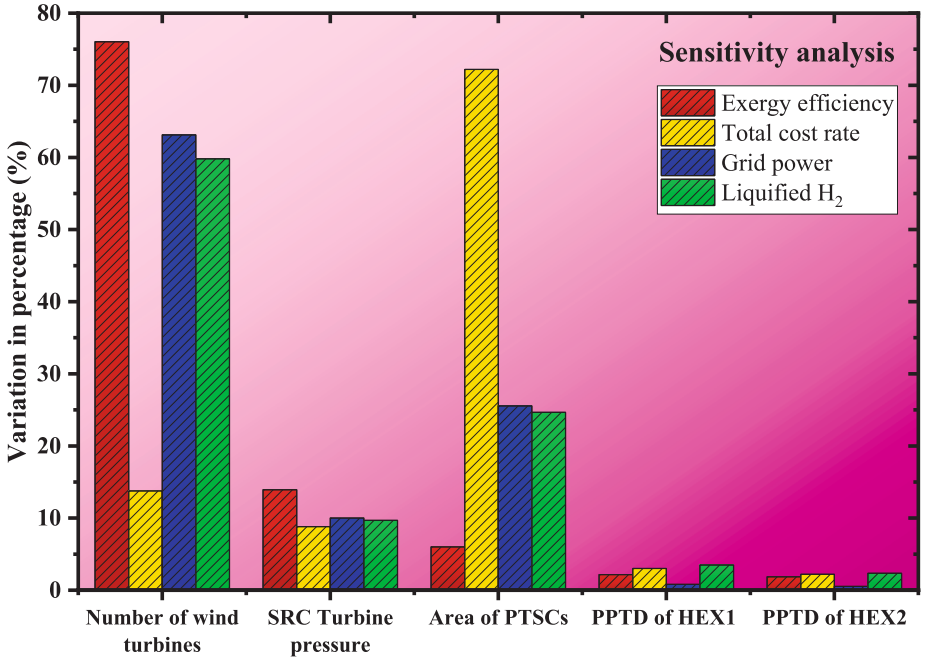

Fig. 6. Sensitivity analysis of the selected parameters on the system's outputs.

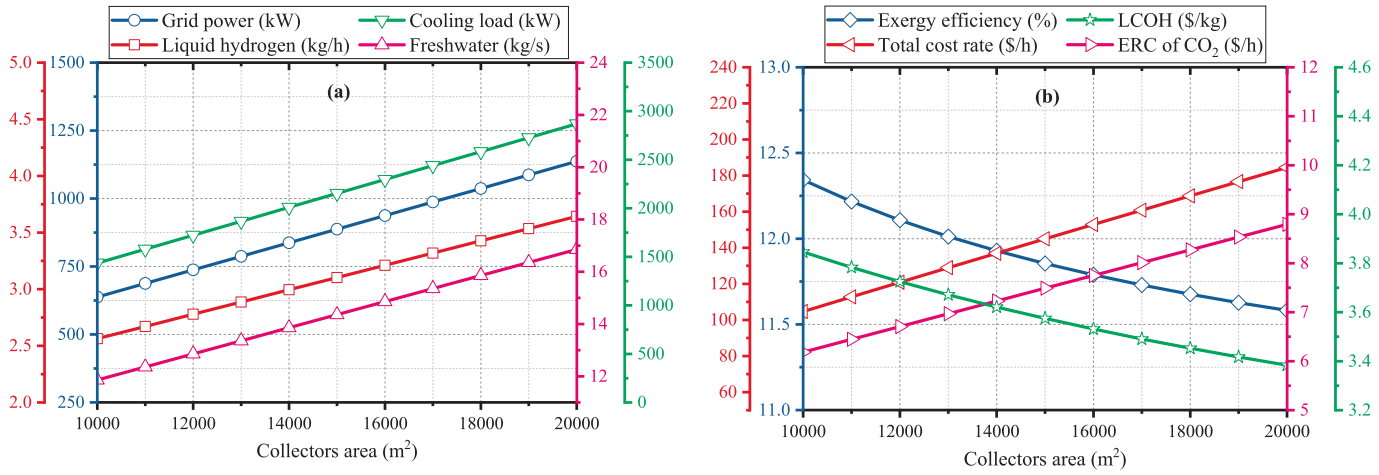

Fig. 7. Impact of increasing total area of PTSCs on the performance indicators of the system.

and hydrogen production (59.82%), highlighting its crucial role in stabilizing renewable electricity supply and reducing reliance on auxiliary power sources. In parallel, the PTSC area shows a major effect on the total cost rate (72.20%) and notable influence on grid power (25.54%) and hydrogen output (24.66%), since solar collection capacity directly governs thermal energy availability for the SRC, ARC, ORC, and liquefaction cycles. In contrast, operational parameters such as the SRC turbine pressure (8.81–13.93%) and the pinch-point temperature differences of HEX1 and HEX2 (0.52–3.49%) exhibit relatively minor sensitivities, indicating that thermodynamic fine-tuning of heat exchangers and cycle pressures yields limited system-wide influence compared to the scale of renewable resource inputs. Overall, the sensitivity trends underscore that system performance is predominantly dictated by renewable energy capacity sizing, while internal cycle parameters exert secondary effects.

6.2. Parametric analysis

A detailed analysis is conducted to assess how critical system parameters affect overall performance. Their effects on system outputs, efficiency, and economic and environmental indicators are systematically assessed.

- **Solar field size**

Fig. 7(a) presents the impact of enlarging the total PTSCs area on the outputs of the hybrid multi-generation system. Increasing the collector surface from 10,000 to 20,000 m^2 captures more solar energy, elevating the heat absorbed by the circulating fluid. This higher thermal input raises the outlet temperature and heat transfer in HEX1, generating more steam in the SRC and boosting turbine work. Consequently, the electrical output rises from 637.57 kW to 1,136.83 kW. The amplified thermal energy also enhances the ARC cooling capacity, nearly doubling it from 1,434.71 kW to 2,869.89 kW. Additionally, the increased power availability enables greater hydrogen production via the PEME, increasing liquefied hydrogen output to 3.64 kg/h, while the RO desalination unit produces up to 16.85 kg/h of freshwater. These results highlight the strong interdependence between solar input and multi-

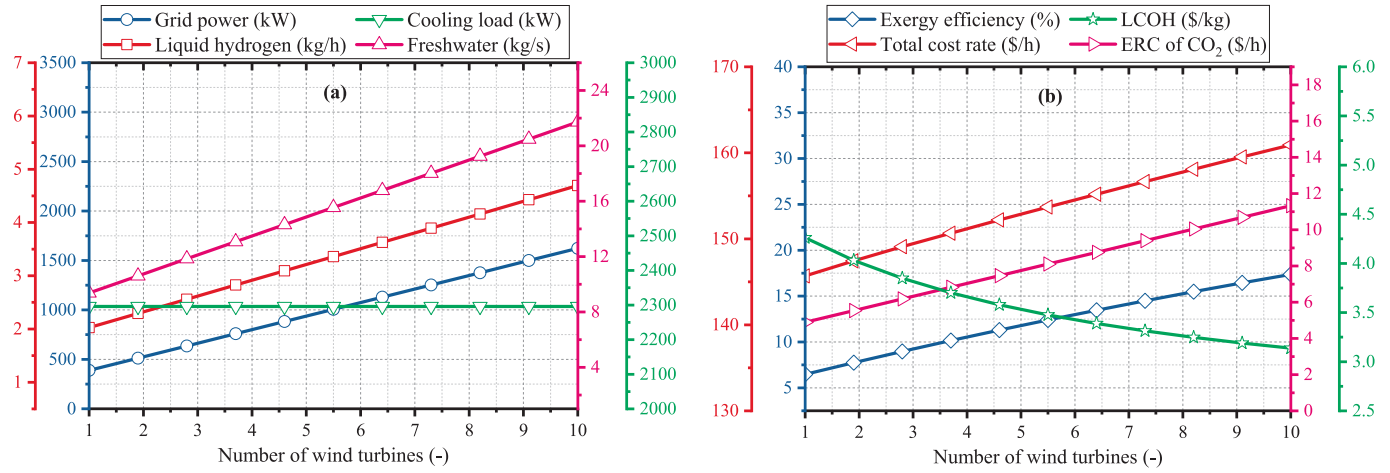

Fig. 8. Impact of increasing number of wind turbines on the performance indicators of the system.

product energy generation.

However, Fig. 7(b) shows that expanding the PTSC area introduces thermodynamic and economic trade-offs. Higher heat exchanger temperatures lead to increased entropy generation, slightly lowering overall exergy efficiency from 12.34% to 11.58%. Economically, additional collectors and larger heat exchangers raise the system's operating cost from 104.61 $/h to 184.46 $/h. Despite this, the LCOH drops from 3.84 $/kg to 3.38 $/kg, as higher hydrogen output offsets the added investment. Environmentally, a larger solar field improves renewable energy utilization and reduces reliance on fossil fuels, enhancing CO_2 mitigation potential.

- **Wind turbine count**

The wind farm is a key contributor to the hybrid wind–solar multi-generation system, directly affecting electricity supply and subsequent subsystem operations. As shown in Fig. 8(a), raising the number of turbines from 1 to 10 boosts the total grid-connected electricity from 388.74 kW to 1,622.61 kW. This increase not only ensures a larger share of renewable electricity but also sustains continuous operation of the RO desalination unit, enhancing freshwater output from 9.36 kg/h to 21.71 kg/h. Simultaneously, the additional power allocated to the PEME elevates liquefied hydrogen production by roughly 132.17%, while the ARC cooling load remains relatively constant, given its thermal energy demand is independent of wind capacity.

Fig. 8(b) illustrates the impact on thermodynamic performance, where exergy efficiency rises significantly from 6.46% to 17.37% with more turbines. This improvement results from the greater proportion of renewable energy effectively converted into useful outputs and the reduction of subsystem irreversibilities. While these benefits improve electricity, hydrogen, and freshwater production and enhance overall sustainability, they come at the cost of higher capital and operational expenditures, with total costs increasing by about 11.7% due to additional turbine investment and maintenance. Nevertheless, the LCOH decreases by approximately 26.3%, as the substantial rise in hydrogen output offsets the higher expenses. Environmentally, expanding wind capacity reduces reliance on fossil fuels, lowering greenhouse gas emissions and contributing to a cleaner energy profile.

- **SRC turbine inlet pressure**

The inlet pressure of the SRC turbine plays a pivotal role in defining the thermodynamic, economic, and environmental performance of the hybrid system. As depicted in Fig. 9(a), elevating the turbine inlet pressure from 1,000 kPa to 3,500 kPa raises the specific enthalpy of steam entering the turbine, enhancing the expansion potential and increasing mechanical work output. This improvement translates to a rise in grid-connected electricity from 861.26 kW to 1,056.81 kW and a boost in the ARC cooling capacity from 2,126.58 kW to 2,609.43 kW. The additional electricity also supports higher auxiliary production, raising liquefied hydrogen output to 3.47 kg/h and freshwater generation to 16.05 kg/s.

Economically, higher turbine inlet pressures require more robust turbine construction, slightly increasing investment and operational

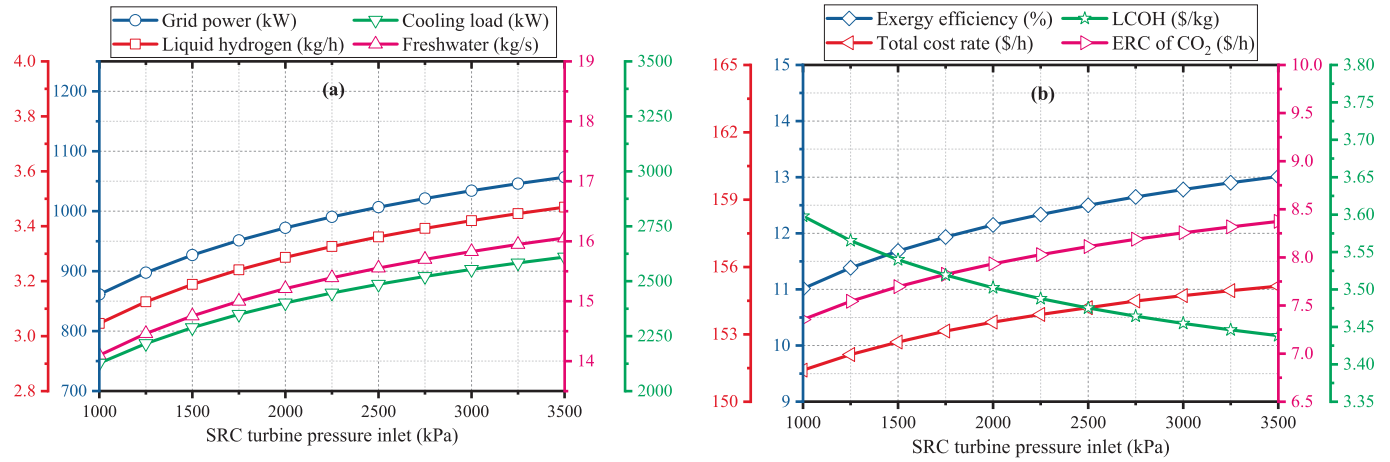

Fig. 9. Impact of increasing SRC turbine inlet pressure on the performance indicators of the system.

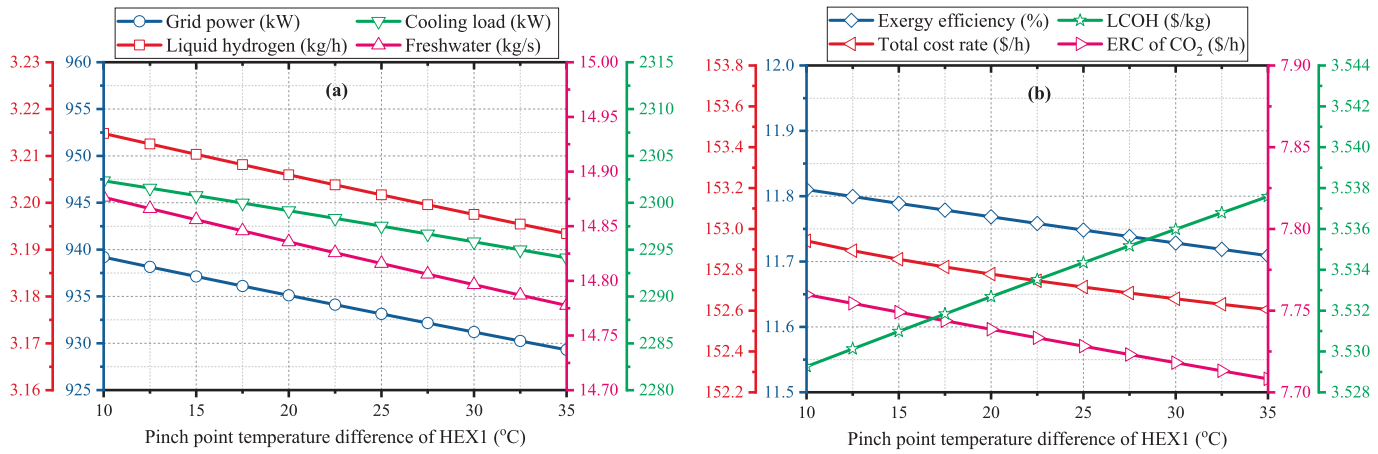

Fig. 10. Impact of increasing PPTD of HEX1 on the performance indicators of the system.

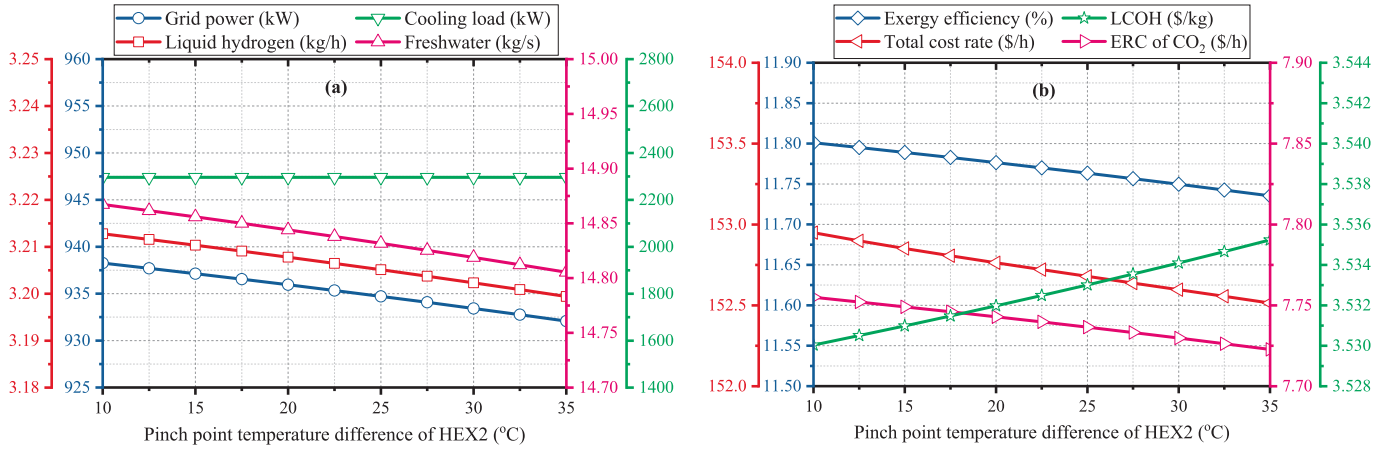

Fig. 11. Impact of increasing PPTD of HEX2 on the performance indicators of the system.

costs. Fig. 9(b) shows total system costs rising modestly from 151.4 $/h to 155.14 $/h, while the LCOH declines from 3.59 $/kg to 3.43 $/kg due to enhanced hydrogen production, improving overall economic viability. Thermodynamically, the increased pressure enhances energy conversion efficiency, reduces cycle irreversibilities, and raises exergy efficiency from 11.01% to 13.01%, indicating better utilization of high-grade thermal energy. Environmentally, improved turbine performance decreases dependence on fossil-fuel backup, contributing to lower greenhouse gas emissions and reinforcing the system's sustainability.

- **Pinch point temperature difference of HEX 1**

The pinch point temperature difference (PPTD) of the HEX1 plays a significant role in shaping the thermodynamic and economic behavior of the system. As illustrated in Fig. 10(a), increasing the PPTD from 10 °C to 35 °C reduces the effective temperature gradient available for heat transfer, thereby lowering the energy delivered from the solar field to the SRC. This reduction directly diminishes turbine expansion work, leading to a drop in net grid-connected power from 939.18 kW to 929.29 kW. The decrease in electricity availability also restricts the operation of the PEME and RO desalination unit, resulting in a slight decline in liquefied hydrogen production (from 3.214 kg/h to 3.193 kg/h) and freshwater output (from 14.876 kg/s to 14.777 kg/s). Furthermore, the cooling load generated by the ARC decreases marginally (about 0.36%) due to the weaker recovery of waste heat.

As depicted in Fig. 10(b), the higher PPTD also leads to a modest reduction in system exergy efficiency, dropping by approximately 0.11%. This decline is attributed to greater thermodynamic irreversibility across the heat exchanger, as a larger temperature approach reduces the quality of recovered thermal energy. From an economic standpoint, however, the rise in PPTD slightly reduces the overall cost rate, decreasing from 152.94 $/h to 152.6 $/h, primarily because a looser pinch point allows for smaller heat exchanger surface areas and less demanding design specifications. Additionally, the LCOH increases from 3.529 $/kg to 3.537 $/kg, since the reduction in hydrogen output outweighs the marginal savings in component costs.

- **Pinch point temperature difference of HEX 2**

The PPTD of HEX2, which couples the solar thermal cycle with the ORC-TEG unit, exerts a noticeable influence on overall system performance. As shown in Fig. 11(a), enlarging the PPTD from 10 °C to 35 °C weakens the driving force for heat transfer, thereby limiting the thermal energy transmitted to the ORC-TEG subsystem. This diminished input lowers both ORC turbine expansion work and the supplementary electricity generated by the TEG, which collectively reduces the net grid-connected power from 938.26 kW to 932.07 kW. The decline in available electrical energy also constrains the performance of the hydrogen production and desalination units, leading to small but measurable reductions in liquefied hydrogen output (3.212 to 3.199 kg/h) and freshwater production (14.867 to 14.805 kg/s). In contrast, the ARC remains unaffected since its driving heat source is independent of HEX2.

As indicated in Fig. 11(b), increasing the PPTD of HEX2 induces a mild decrease in overall system exergy efficiency, with a drop of about

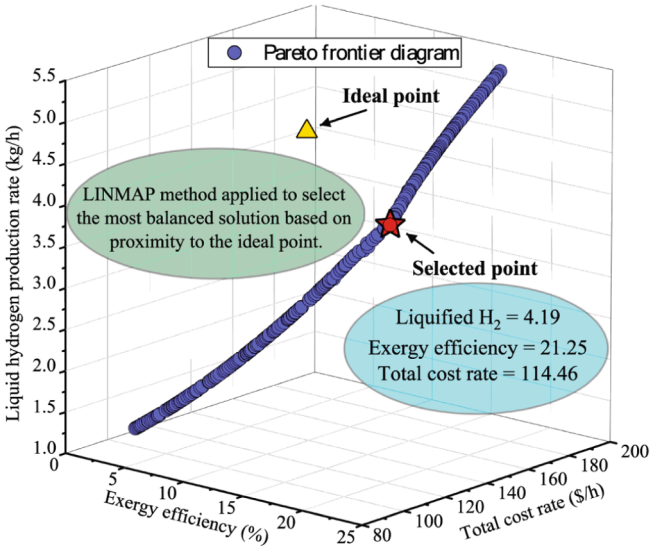

Fig. 12. Pareto frontier diagram in 3D perspective.

0.08%. This effect arises from heightened entropy generation and irreversibility within the heat exchanger, which diminish the quality of thermal energy transferred to the ORC-TEG unit. Economically, a larger PPTD slightly lowers the system's cost rate (152.94 $/h to 152.51 $/h), mainly due to the reduced requirement for heat exchanger surface area and simplified equipment design. However, this minor cost advantage is offset by reduced hydrogen productivity, resulting in a marginal rise in the LCOH from 3.530 $/kg to 3.536 $/kg.

6.3. Optimization results

Identifying optimal operating conditions is a fundamental step in the design and operation of advanced hybrid energy systems, as it ensures both technical performance and economic feasibility. In this study, a hybrid optimization strategy was developed by integrating an ANN with the NSGA-II. This combination enables efficient exploration of the multidimensional solution space to determine optimal system parameters while substantially reducing the computational burden typically associated with iterative multi-objective optimization based on full MATLAB simulations. The ANN accurately captures the nonlinear interactions within the system, allowing rapid evaluation of a wide range of operational scenarios without the need for repeated full-scale simulations. Hyperparameter tuning and cross-validation were performed during training, which ran for up to 1000 epochs. The model achieved excellent predictive accuracy, with coefficients of determination (R2) of 0.99998 for exergy efficiency, 0.99898 for total cost rate, and 0.99995 for liquefied hydrogen production rate. Additionally, the overall MSE was 0.00681. The results highlight the model's reliability as a high-fidelity surrogate.

The optimization targeted three critical performance indicators: total exergy efficiency, liquefied hydrogen production rate, and total cost rate, reflecting the system's combined thermodynamic and economic performance. NSGA-II was employed to identify the Pareto-optimal solutions, representing the best trade-offs among competing objectives. To pinpoint the solution closest to the ideal operating point, the linear programming technique for multidimensional analysis of preference (LINMAP) was applied. LINMAP evaluates each Pareto solution by calculating the Euclidean distance from an ideal reference, enabling the selection of the configuration that achieves the most balanced compromise between efficiency, hydrogen output, and cost. The resulting Pareto frontier, shown in Fig. 12, highlights the trade-offs among system metrics, and Table 11 summarizes the optimized decision variables and corresponding outputs under optimized system configuration.

Table 11
System results under optimum condition.

Parameter	Value
Decision variables	
Number of wind turbines (−)	10
Total area of PTSCs (m^2)	10031.58
Turbine inlet pressure,(kPa)	3300.25
Pinch point temperature differences of HEX1 (°C)	10.02
Pinch point temperature differences of HEX2 (°C)	16.61
Outputs	
$\dot{W}_{wt}(kW)$	1655.4
$\dot{W}_{SRC}(kW)$	501.97
$\dot{W}_{ORC}(kW)$	143.07
$\dot{W}_{TEG}(kW)$	43.67
$\dot{W}_{Grid}(kW)$	1393.5
$\dot{Q}_{Cooling}(kW)$	1375.9
$\dot{m}_{freshwater}(kg/s)$	19.42
$\dot{m}_{Liquid-H2}(kg/h)$	4.19
$LCOH(\$/kg)$	3.24
$\dot{E}x_{D,total}(MW)$	7.78
$\eta_{ex}(\%)$	21.25
$\dot{Z}_{tot}(\$/h)$	114.46
$ERC_{CO_2}(\$/h)$	10.12

By comparing the results after optimization (Table 11) with those under base conditions (Table 9), significant improvements are observed across technical, economic, and environmental indicators. The optimized system achieves a net grid power of 1393.5 kW, representing a 48.7% increase compared to the base case (937.13 kW). Freshwater production rises substantially from 14.86 kg/s to 19.42 kg/s (a 30.7% improvement), while liquefied hydrogen generation increases from 3.21 kg/h to 4.19 kg/h (a 30.5% improvement), underscoring the strengthened role of hydrogen as a clean energy carrier. The exergy efficiency nearly doubles, improving from 12.11% to 21.25%, while total exergy destruction decreases from 9.91 MW to 7.78 MW, confirming the effectiveness of optimization in reducing irreversibilities.

From an economic perspective, the total cost rate drops from 162.69 $/h to 114.46 $/h (a 29.6% reduction), while the LCOH decreases from 3.53 $/kg to 3.24 $/kg, reflecting the combined effect of higher hydrogen output and reduced operating costs. Environmentally, the system also benefits: CO_2 emissions cost reduction is evident, with ERC_{CO_2} decreasing from 7.75 $/h to 10.12 $/h. Although the cooling load decreases from 2295.8 kW to 1375.9 kW due to thermodynamic redistribution among subsystems, this trade-off is offset by the significant improvements in electricity, hydrogen, and freshwater outputs. Overall, optimization enhances the system's technical efficiency, economic viability, and environmental performance.

6.4. Case study: Application to urban green energy buildings in Dammam

To evaluate the practical implementation of the proposed hybrid wind–solar multi-generation system, a case study was conducted using real meteorological data from Dammam, Saudi Arabia. The city's rapidly expanding urban districts face increasing demand for electricity, cooling, and potable water, alongside growing interest in low-carbon energy solutions for sustainable building operations. A centralized district cogeneration approach, integrating solar and wind resources, offers a promising pathway to meet these needs while simultaneously producing green hydrogen for on-site storage and distributed fueling. This case study demonstrates the application of the developed general modeling framework to a specific location; the methodology is fully reproducible and can be adapted to assess system performance in other regions with distinct climatic and economic conditions.

Dammam, a coastal city in Saudi Arabia, exhibits exceptionally high solar irradiation and moderate wind potential, making it an ideal location for hybrid renewable deployment. By combining parabolic trough

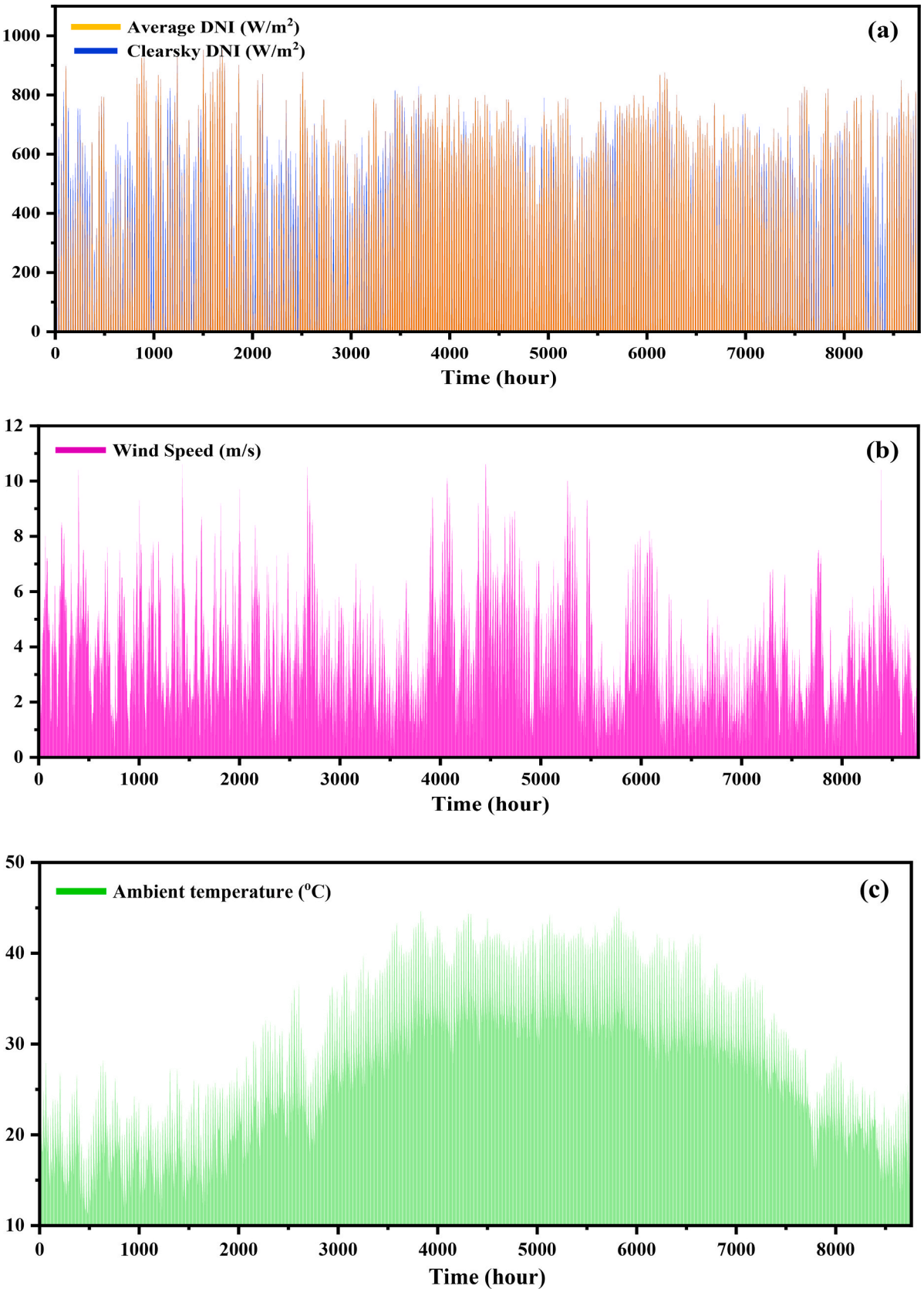

Fig. 13. Hourly meteorological data for Dammam, Saudi Arabia, in 2019: (a) Average and clear sky DNI in $[W/m^2]$, (b) wind speed in $[m/s]$, and (c) ambient temperature in $[^{\circ}C]$.

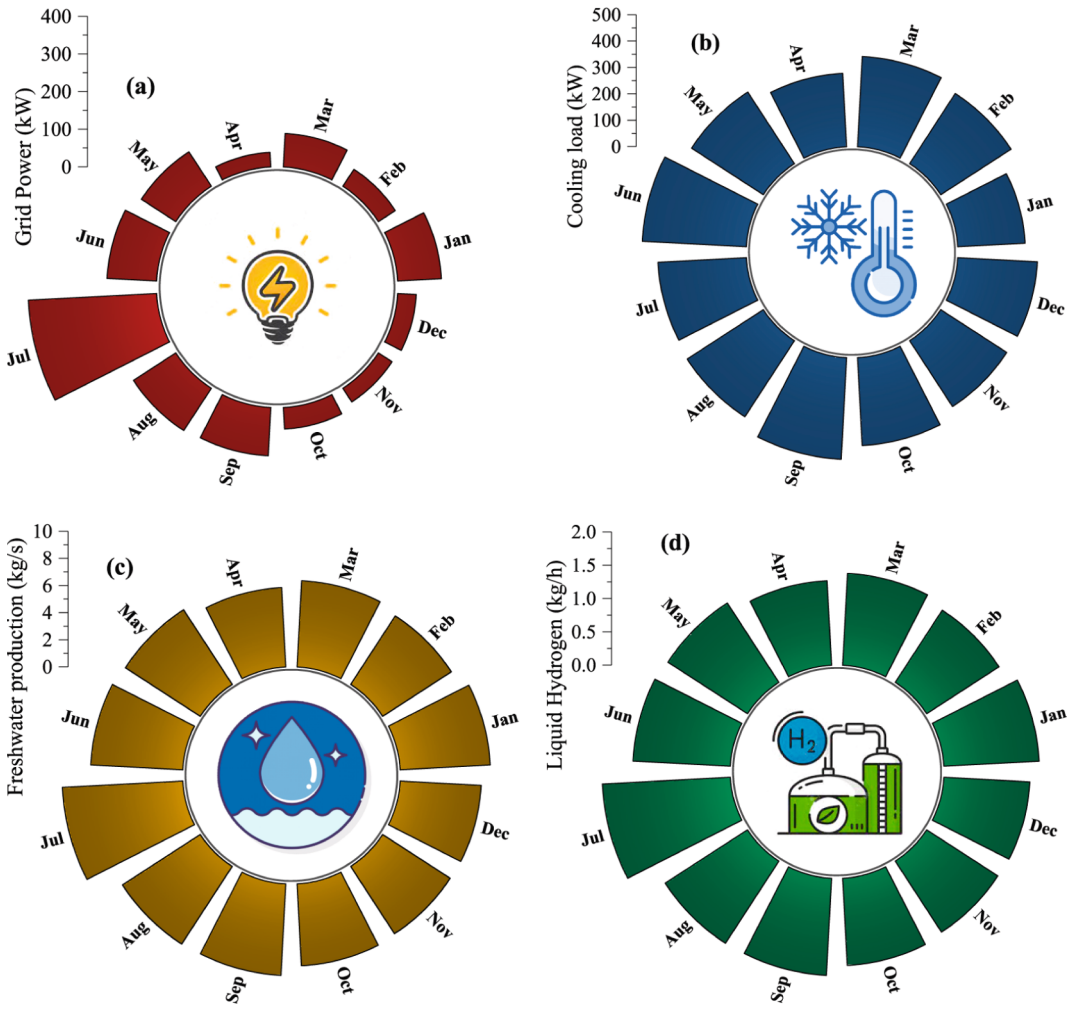

Fig. 14. Monthly outputs of the proposed multi-generation system: (a) grid power, (b) cooling load, (c) freshwater production, and (d) liquefied hydrogen output.

solar collectors with wind turbines, the proposed system captures complementary energy streams, ensuring reliable electricity supply even during intermittent solar conditions. The recovered thermal energy drives steam Rankine and organic Rankine cycles, while low-grade heat supports single-effect absorption cooling and reverse osmosis desalination. The integration of a PEM electrolyzer and hydrogen liquefaction unit provides a clean, storable fuel for district-scale applications, such as electrified transportation or backup energy for green buildings. Fig. 13 presents the hourly variations of wind speed, solar irradiance, and ambient temperature in Dammam during 2019, which serve as fundamental inputs for the operation of the proposed hybrid system. The meteorological dataset, sourced from the National Solar Radiation Database [75], highlights the city's strong solar potential complemented by moderate wind resources, making it well-suited for hybrid renewable energy deployment.

Fig. 14(a–d) presents the monthly average outputs of the proposed multi-generation system, illustrating the distinct seasonal responses of electricity, cooling, freshwater, and liquefied hydrogen production under realistic meteorological conditions. Grid electricity output (Fig. 14a) exhibits the strongest seasonal variability, ranging from 38.7 kW in April to 340.4 kW in July. This nearly ninefold increase is primarily driven by the combined availability of solar irradiance and wind resources, confirming the dominant role of renewable inputs in supplying high-temperature heat to the power generation cycles.

The cooling output of the absorption refrigeration cycle (Fig. 14b) follows a different seasonal trend, peaking at 393.8 kW in June. This behavior is governed mainly by ambient temperature rather than solar availability, reflecting the thermodynamic dependence of the LiBr–H_2O absorption system on heat rejection conditions. Freshwater production (Fig. 14c), which is electrically driven through the reverse osmosis unit, varies between 5.86 and 8.88 m^3/h and closely tracks the availability of grid electricity.

Liquefied hydrogen production (Fig. 14d) represents the most critical and distinguishing output of the system, as it integrates the performance of renewable electricity generation, PEME, and the Claude-based liquefaction cycle enhanced by LNG cold energy recovery. The hydrogen output varies from a minimum of 1.27 kg/h during low-resource months (April and November) to a maximum of 1.92 kg/h in July, corresponding to a seasonal increase of approximately 51%. Notably, this variation is substantially smaller than that observed for grid electricity, indicating a strong buffering effect introduced by system integration.

The July peak in liquefied hydrogen production is primarily attributed to the simultaneous availability of surplus renewable electricity for PEME and improved thermodynamic performance of the liquefaction train. In particular, the utilization of LNG cold energy for hydrogen precooling significantly reduces the specific compression and refrigeration work required in the Claude cycle. This effect becomes more pronounced during summer months, when higher cooling loads and increased waste-heat recovery enhance the performance of the ORC–TEG–LNG thermal cascade supplying the cryogenic stages.

The relatively smooth seasonal profile of liquefied hydrogen production demonstrates that, unlike direct electricity output, hydrogen liquefaction benefits from inherent energy storage and thermal

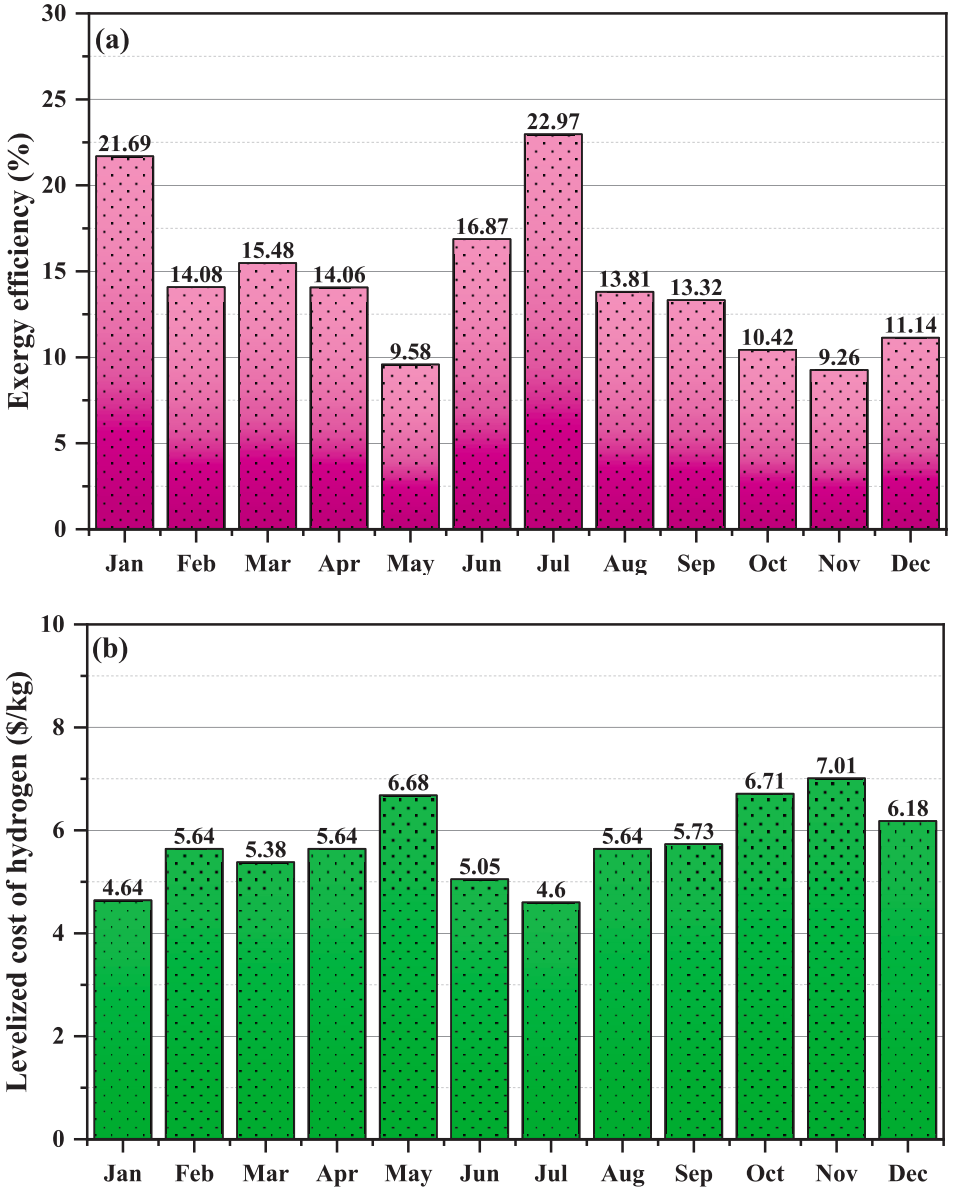

Fig. 15. Monthly assessment of system performance metrics: (a) exergy efficiency, (b) levelized cost of hydrogen, and (c) emissions reduction costs.

integration mechanisms. Variable renewable inputs are effectively transformed into a storable, high–energy–density fuel through coordinated use of waste heat and cryogenic cold energy. This confirms the effectiveness of the proposed design in stabilizing hydrogen supply at the district scale while maximizing overall system efficiency.

Fig. 15 illustrates the monthly variation in key performance indicators, demonstrating the strong seasonal dependency of the proposed hybrid system. Exergy efficiency peaks in July (22.97%) and January (21.69%), driven by higher wind availability and improved thermodynamic conditions, while its lowest values occur in November (9.26%) and May (9.58%), reflecting reduced renewable input and lower thermal resource intensity. The LCOH exhibits an inverse trend, reaching its minimum in July (4.60 $/kg) and maximum in November (7.01 $/kg), primarily linked to fluctuations in renewable electricity supply that directly affect electrolyzer utilization. Emission reduction costs show pronounced variability, with a significant peak in July (6.38 $/kg CO_2-eq) due to enhanced displacement of fossil-based generation, and minimum values in November (2.04 $/kg CO_2-eq) when system performance is at its lowest. The total cost rate demonstrated minimal seasonal fluctuation, remaining within a narrow range of approximately 152.5 to 157.9 $/h throughout the year, as the system's capital costs are dominant and largely invariant to monthly output variations. Overall, the monthly analysis confirms that seasonal renewable resource availability governs both thermodynamic efficiency and economic–environmental outcomes of the integrated system.

Overall, the findings confirm that a centralized hybrid cogeneration system can enhance urban energy resilience, reduce dependence on fossil fuels, and provide distributed low-carbon services. By enabling integrated electricity, cooling, water, and hydrogen production for multiple buildings, the approach supports sustainable urban development and aligns with Saudi Arabia's Vision 2030 objectives of energy diversification, decarbonization, and promotion of hydrogen as a strategic clean energy carrier.

7. Conclusion

This study developed and assessed an advanced wind–solar–driven cogeneration system tailored to support net-zero-energy green buildings

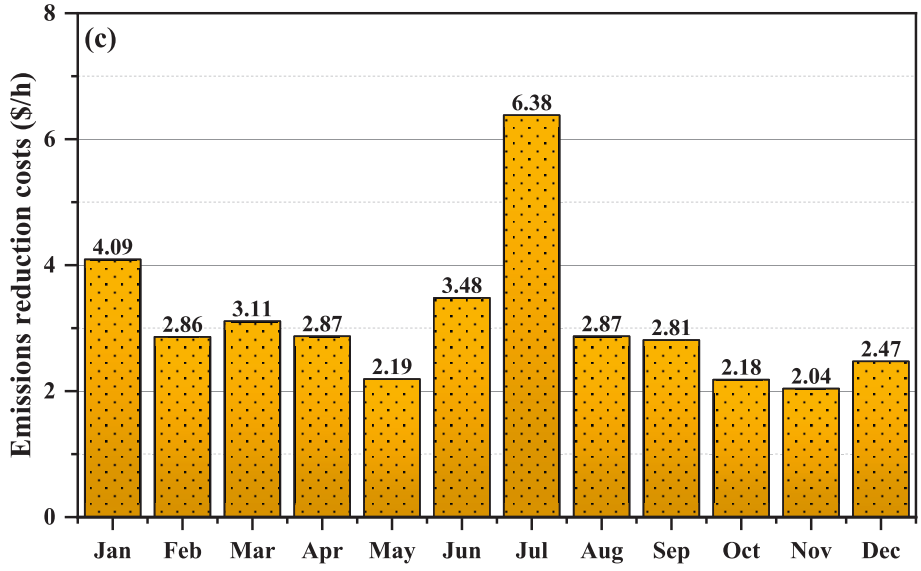

Fig. 15. (*continued*).

by supplying multiple end-use demands, including electricity, cooling, freshwater, and liquefied green hydrogen. The integrated configuration employed wind turbines, parabolic trough solar collectors, an LNG regasification unit, an SRC, an ORC coupled with a TEG unit, an ARC, a PEME, an RO desalination module, and a Claude-based hydrogen liquefaction cycle. Through synergistic waste heat recovery, thermal cascading, and hybridization of renewable sources, the system was engineered to enhance building-level energy resilience, minimize primary energy consumption, and reduce operational emissions. A comprehensive thermo-economic–environmental assessment and an optimization process using NSGA-II and an ANN-based surrogate model enabled high-fidelity performance evaluation with markedly reduced computational cost. A case study for Dammam, Saudi Arabia, validated system applicability under real climatic conditions. The key findings are summarized as follows:

- The proposed system configuration effectively harnesses LNG cold exergy to significantly enhance the efficiency of the hydrogen liquefaction process, a key enabler for practical hydrogen storage at the district scale.
- Parametric studies quantified the dominant influence of renewable resource capacity: expanding the PTSC field from 10,000 to 20,000 m^2 raised grid power by 78% (to 1.14 MW) and hydrogen output to 3.64 kg/h, while increasing wind turbines from 1 to 10 boosted grid power by 317% (to 1.62 MW) and hydrogen production by 132%.
- Under optimal operating conditions identified by the ANN-NSGA-II framework, the system achieves a substantial improvement over the baseline, with a 48.7% increase in net power output (1.39 MW), a 30.5% rise in liquefied hydrogen production (4.19 kg/h), a 75% enhancement in exergy efficiency (21.25%), and a 29.6% reduction in total cost rate. The levelized cost of hydrogen reaches a competitive 3.24 $/kg under these conditions.
- The surrogate-based optimization framework effectively reduced computational time of multi-objective optimization while maintaining high predictive accuracy ($R^2 > 0.998$).
- A detailed case study for Dammam, Saudi Arabia, utilizing real meteorological data, demonstrated the system's real-world applicability. While grid power exhibited an 8.8-fold seasonal variation (38.7 to 340.4 kW), liquefied hydrogen production showed a more stable 51% variation (1.27 to 1.92 kg/h). This moderation demonstrates the system's capability to buffer renewable intermittency and deliver a reliable, storable fuel.
- The developed thermodynamic modeling and data-driven optimization framework is general and fully reproducible. It provides an adaptable tool for assessing the techno-economic feasibility of such integrated systems in other geographical regions with distinct climatic conditions and energy market contexts.

In conclusion, this work demonstrates that tightly integrating renewable generation with LNG cold recovery and multi-stage waste heat utilization presents a technically sound and economically promising strategy for developing resilient, multi-service energy infrastructures for future sustainable cities. The pathway toward implementation now extends to dynamic performance analysis under transient conditions, integration with smart building and grid management systems, and detailed lifecycle assessments to further validate long-term sustainability and scalability across diverse global contexts.

CRediT authorship contribution statement

Ling Ji: Writing – review & editing, Writing – original draft, Investigation. **Ali Basem:** Investigation, Formal analysis. **Hyder H. Abed Balla:** Investigation, Data curation. **Omar J. Alkhatib:** Supervision, Methodology, Conceptualization. **Khalid Alkhattabi:** Formal analysis, Data curation. **Yonghui Li:** Writing – review & editing, Supervision, Resources. **M.A. Ahmed:** Project administration, Funding acquisition. **Mohana Alanazi:** Validation, Data curation. **Hind Albalawi:** Writing – original draft, Resources, Funding acquisition. **Ibrahim Mahariq:** Writing – review & editing, Writing – original draft, Validation, Supervision.

Declaration of competing interest

The authors declare that they have no known competing financial interests or personal relationships that could have appeared to influence the work reported in this paper.

Acknowledgement

Princess Nourah bint Abdulrahman University Researchers Supporting Project number (PNURSP2026R29), Princess Nourah bint Abdulrahman University, Riyadh, Saudi Arabia. The authors extend the appreciation to the Deanship of Postgraduate Studies and Scientific Research at Majmaah University for funding this research work through

the project number (R-2026-30). This work was financially supported by the National Social Science foundation project (23BJL088); the General Project of “Research Center for Cultural and Tourism Integration” (a key base of philosophy and social sciences in Sichuan Province): “Research on the Path of Fintech to Solve the 'Integration Effect Paradox' in Chengdu-Chongqing Cultural and Tourism Industry Driven by Technology-Institution Coordination (WL2025138)”.

Data availability

The authors do not have permission to share data.

References

[1] Gai Z, Li P, Shen Y, Zhang R, Wan Z, Liu M, et al. Systematic evaluation of a high-performance solar-driven hybrid system for cost-effective methanol and hydrogen co-production via chemical looping methane reforming. Fuel 2025;393:134925. https://doi.org/10.1016/j.fuel.2025.134925.
[2] Deng Y, Dai H, Zhao C, Yuan J, Liu W, Yin R, et al. Research on the carbon neutrality path of urban block buildings through multi-dimensional synergy. J Build Eng 2025;114:114391. https://doi.org/10.1016/j.jobe.2025.114391.
[3] Hai T, Zoghi M, Javaherdeh K. 4E analysis and optimization of a biomass-fired waste-to-energy plant integrated with a compressed air energy storage system for the multi-generation purpose. Fuel 2023;348:128457. https://doi.org/10.1016/j.fuel.2023.128457.
[4] Feili M, Haghghi MA, Ghaebi H, Athari H. A data-driven multi-criteria optimization of a biogas-fed s-graz cycle combined with biogas steam reforming and Claude cycle for sustainable hydrogen liquefaction. Fuel 2025;390:134700. https://doi.org/10.1016/j.fuel.2025.134700.
[5] Hu S, Zhang L, Zhang Y. Optimization of rural integrated energy system with shared energy storage on multiple-timescales. Commun Comput Inf Sci 2025; 2182. https://doi.org/10.1007/978-981-97-7004-5_16. CCIS:217–31.
[6] Li L, Zhang C, Xia H, Duan M, Yang J. Simulation of economic, energy-saving, and environmental benefits of the centralized-decentralized two-stage heating mode. Energ Buildings 2025;341:115869. https://doi.org/10.1016/j.enbuild.2025.115869.
[7] Soltanifar F, Bahrami A, Sohani A. A green energy-economic optimized solar driven solution for power, methanol, and hydrogen production together. Fuel 2025;386:134147. https://doi.org/10.1016/j.fuel.2024.134147.
[8] Akbarnataj K, Saffaripour M, Houshfar E. Membrane-based CO2 capture integrated with CCHP for a nearly zero-carbon building. Build Environ 2025;273:112738. https://doi.org/10.1016/j.buildenv.2025.112738.
[9] Sharifishourabi M, Dincer I, Mohany A. Development and assessment of a new solar-geothermal based integrated energy system with sonic hydrogen generation for buildings. J Build Eng 2023;80:107944. https://doi.org/10.1016/j.jobe.2023.107944.
[10] Chen Y, Quan M, Wang D, Tian Z, Zhuang Z, Liu Y, et al. Energy, exergy, and economic analysis of a solar photovoltaic and photothermal hybrid energy supply system for residential buildings. Build Environ 2023;243:110654. https://doi.org/10.1016/j.buildenv.2023.110654.
[11] Park BR, Young Kim A, Choi EJ, Jun Y, Moon JW. Evaluation of the energy and environmental performance of a novel BIPV window system for net-zero energy buildings. Energ Buildings 2025;348:116453. https://doi.org/10.1016/j.enbuild.2025.116453.
[12] Meng Q, He Y, Hussain S, Lu J, Guerrero JM. Day-ahead economic dispatch of wind-integrated microgrids using coordinated energy storage and hybrid demand response strategies. Sci Rep 2025;15:26579. https://doi.org/10.1038/s41598-025-11561-2.
[13] Meng Q, He Y, Hussain S, Lu J, Guerrero JM. Low carbon optimization for wind integrated power systems with carbon capture and energy storage under carbon pricing. Sci Rep 2025;15:32714. https://doi.org/10.1038/s41598-025-17463-7.
[14] Yang Y, Yan G, Mu G, Chen Z. Hierarchical bidding strategy for heterogeneous P2H loads and wind power: state-driven aggregation and switching time scheduling. Energy 2025;334:137766. https://doi.org/10.1016/j.energy.2025.137766.
[15] Ghanbari K, Maleki A, Rezaei OD. Optimal design of solar/wind/energy storage system-powered RO desalination unit: Single and multi-objective optimization. Energy Convers Manag 2024;315:118768. https://doi.org/10.1016/j.enconman.2024.118768.
[16] Zhang Z, Ma K, Chen Y, Yang K, Guo W, Lund PD. Optimization of a solar-wind-gas driven cooling and power system through multi-device coordination and dual energy storage: demand response and exergo-environmental cost analysis. Energy Convers Manag 2025;346:120457. https://doi.org/10.1016/j.enconman.2025.120457.
[17] Zhang Y, Liang Z, Luo X, Liang Y, Lu P, Chen J, et al. Performance analysis and optimization of a methanol steam reforming proton exchange membrane fuel cell based trigeneration system via carbon capture for near-zero carbon emission production. Fuel 2025;390:134649. https://doi.org/10.1016/j.fuel.2025.134649.
[18] Boujelbene M, Hassan WH, Farouk N, Soliman NF, Marouani I, Abduvokhidov A, et al. Data-driven optimization and 4E analysis of a novel LNG-integrated gas turbine-based system using ANN-GA hybrid approaches: enhanced hydrogen production and CO2 capture for energy applications. Fuel 2026;407:137283. https://doi.org/10.1016/j.fuel.2025.137283.
[19] Abed AM, Shawabkeh A, Jhala R, Ramachandran T, Shankhyan A, Mann VS, et al. Exergoeconomic investigation of a multi-generation system based on gas turbine, carbon dioxide recondensation, multi effect desalination and methanol-steam reforming. Therm Sci Eng Prog 2025;58:103170. https://doi.org/10.1016/j.tsep.2024.103170.
[20] Khanmohammadi S, Atashkari K. Energy, exergy, and environmental analyses of a poly-generation system based on biomass gasification. Fuel 2022;320:123963. https://doi.org/10.1016/j.fuel.2022.123963.
[21] Ji L, Basem A, Abed Balla HH, Li Y, Alkhatib OJ, Ayadi M, et al. Thermo-economic decision-making and intelligent optimization of a sustainable biogas-driven system with integrated peak demand management. Biomass Bioenergy 2026;207:108785. https://doi.org/10.1016/j.biombioe.2025.108785.
[22] Almadhor A, Samad S, Shaban M, Abed AM, Alhomayani FM, Abduvalieva D, et al. An eco-friendly multi-generation system integrating geothermal-driven power and cooling cycles with LNG regasification and hydrogen production: a thermo-economic optimization. Appl Therm Eng 2025;277:126973. https://doi.org/10.1016/j.applthermaleng.2025.126973.
[23] Shi P, Shang R. Performance evaluation and optimization of a multigeneration hybrid system for power, hydrogen, cooling, and freshwater production from renewable sources. Appl Therm Eng 2024;246:122866. https://doi.org/10.1016/j.applthermaleng.2024.122866.
[24] Zoghi M, Hosseinzadeh N, Gharaie S, Zare A. Waste heat recovery of a combined Brayton and inverse Brayton cycle for gas turbine based multi-generation hydrogen and freshwater purposes: 4E comparison with a simple coupled Brayton and inverse Brayton cycle. Therm Sci Eng Prog 2024;53:102718. https://doi.org/10.1016/j.tsep.2024.102718.
[25] Ekariansyah AS, Muwonge M, Saefuttamam MR, Dikaimana Y, Nasruddin. Energy, exergy, and exergy-economic optimization of a multigeneration system driven by geothermal primary heat source using multi-objective genetic algorithm (MOGA). Energy 2025;330:136653. https://doi.org/10.1016/j.energy.2025.136653.
[26] Sharifishourabi M, Dincer I, Mohany A. A novel energy system designed to cover electricity, heat, hydrogen and propane for decarbonized buildings. Energ Buildings 2025;343:115907. https://doi.org/10.1016/j.enbuild.2025.115907.
[27] Zhang Y, Xu C, Zhou Y, Wang J. Optimal operation of wind-solar-storage-hydrogen system considering multi-scale forecasting of source-load. Energy Convers Manag 2025;344:120296. https://doi.org/10.1016/j.enconman.2025.120296.
[28] Assareh E, Izadyar N, Jamei E, Mobayen S, Abbasi M, Mohammadi H, et al. Application of a multi-objective approach integrating solar-wind co-generation with response surface method to optimize zero-energy buildings. Appl Therm Eng 2025;265:125637. https://doi.org/10.1016/j.applthermaleng.2025.125637.
[29] Imandoust M, Kermani Alghorayshi ST, Zahedi R, Aslani A, Khanqah MQ. Multi-objective optimization of hybrid solar-wind MSF-RO cogeneration desalination systems using NSGA-II to enhancing energy efficiency, cost reduction and sustainability. Sep Purif Technol 2025;378:134740. https://doi.org/10.1016/j.seppur.2025.134740.
[30] Chowdhury P, Das P, Yeassin R, Bonah Agyekum E, Irshied Al-Maaitah M, Odoi-Yorke F. Exploring the potential of solar and wind-powered green hydrogen: production, costs and environmental impacts in South Asia. Int J Hydrogen Energy 2025;137:288–302. https://doi.org/10.1016/j.ijhydene.2025.05.100.
[31] Xiao Q, Zhang L, Zhao L. Multi-aspect analysis and optimization of a novel geothermal-based power, liquefied hydrogen, and freshwater production system. Int J Hydrogen Energy 2024;66:521–39. https://doi.org/10.1016/j.ijhydene.2024.03.344.
[32] Li Wlong, Guo Y, Chen Bming. Research progress on pyrolysis gasification and resource utilization of tobacco waste: Component analysis and recovery strategies. J Anal Appl Pyrol 2026;193:107425. https://doi.org/10.1016/j.jaap.2025.107425.
[33] Taghavi M, Lee CJ. Development of a novel hydrogen liquefaction structure based on liquefied natural gas regasification operations and solid oxide fuel cell: Exergy and economic analyses. Fuel 2025;384:133826. https://doi.org/10.1016/j.fuel.2024.133826.
[34] Liang J, Wu S, Lu T. Portfolio selection and optimal planning for hydrogen energy storage systems composed of heterogeneous electrolyzer and fuel cell technologies in industrial park multi-energy systems. Appl Energy 2026;403:127001. https://doi.org/10.1016/j.apenergy.2025.127001.
[35] Naderi M, Vajdi M, Abdolalipouradl M, Mohammadkhani F. Optimization using RSM of combined cycle of power, NG, and hydrogen production by a bi-geothermal energy resource and LNG heat sink. Case Stud Therm Eng 2025;74:106925. https://doi.org/10.1016/j.csite.2025.106925.
[36] Hu F, Yang H, Zhou X, Zhao S, Qiu L, Wei S, et al. Spatial dynamics of lithium battery recycling enterprises in China: implications for smart waste management and public health. Front Public Heal 2026;13:1729413. https://doi.org/10.3389/fpubh.2025.1729413.
[37] Wang Z, Li J, Salih SQ, Shaban M, Samad S, Almadhor A, et al. Life cycle assessment, exergoenvironmental analysis, and AI-driven optimization of an oxy-biogas power plant combined with liquefied CO2 and H2 generation units. Energy 2025;330:136867. https://doi.org/10.1016/j.energy.2025.136867.
[38] Saadh MJ, Campoverde Santos DK, Oleas Lopez JM, Farajollahi AH, Salgado Tello IP, Sanchez Herrera TE, et al. Energy, exergy, exergoeconomic, and exergoenvironmental analysis of an integrated hydrogen production and liquefaction process using the Allam-Z cycle, SOEC, and cryogenic refrigeration. Int J Hydrogen Energy 2025;100:1246–65. https://doi.org/10.1016/j.ijhydene.2024.12.293.
[39] Hai T, Sharma K, Mahariq I, El-Shafai W, Fouad H, Sillanpää M. A multi-criteria data-driven study/optimization of an innovative eco-friendly fuel cell-heat recovery process, generating electricity, cooling and liquefied hydrogen. Energy 2025;314:134079. https://doi.org/10.1016/j.energy.2024.134079.

[40] Qing X. Solar-driven multi-generation system: thermoeconomic and environmental optimization for power, cooling, and liquefied hydrogen production. Energy 2024; 293:130409. https://doi.org/10.1016/j.energy.2024.130409.
[41] Wei H, Hasanuzzaman M, Selvaraj J. Decision study and ANN-assisted multi-criteria optimization of a novel three-state solar-driven integrated process using energy storage for hydrogen liquefication: a case study for Malaysian solar status. J Energy Storage 2024;99:113216. https://doi.org/10.1016/j.est.2024.113216.
[42] Sun Y, Li HW, Wang D, Du CH. A novel zero emission combined power and cooling system for concentrating solar power: thermodynamic and economic assessments and optimization. Case Stud Therm Eng 2024;58:104406. https://doi.org/10.1016/j.csite.2024.104406.
[43] He D, Li H, Gao R, Li Y, Fan L, Long X, et al. INSL-FLASH: a Fission response function based low-cost adaptive reactor physics code for high-fidelity simulation. Nucl Sci Eng 2025:1–19. https://doi.org/10.1080/00295639.2025.2561327.
[44] Du G, Basem A, Othman NA, Sinnah ZAB, Alhumaid S, Ayadi M, et al. Optimizing thermo/hydro-Diodic performance (T/H-DP) of Tesla valve designs by artificial neural network (ANN) and genetic algorithm (GA); a numerical simulation. Int Commun Heat Mass Transf 2025;169:109711. https://doi.org/10.1016/j.icheatmasstransfer.2025.109711.
[45] Shakeri A, Asadbagi P, Babamiri NA. Techno-economic, techno-environmental assessments, and deep learning optimization of an integrated system for CO2 capturing from a gas turbine: Tehran case study. Energy 2024;306:132438. https://doi.org/10.1016/j.energy.2024.132438.
[46] Boujelbene M, Basem A, Sawwan H, Samad S, Ben Hamida MB, Amari A, et al. Multi-objective optimization of a biogas-fueled multigeneration system with a supercritical CO2-based power and multi-level cooling cycle: a hybrid ANN-MOPSO approach. Fuel 2026;405:136687. https://doi.org/10.1016/j.fuel.2025.136687.
[47] Hijji M. A unified framework for optimizing solar-assisted multi-generational energy systems using the multi-objective dragonfly algorithm and neural networks. Int Commun Heat Mass Transf 2025;169:109515. https://doi.org/10.1016/j.icheatmasstransfer.2025.109515.
[48] Korpeh M, Lotfollahi A, Navid Faraji S, Gharehghani A, Ahmadi S. Machine learning-assisted optimization of a novel hybrid solar-geothermal system supported by proton exchange membrane fuel cell for sustainable and continuous energy supply. Renew Energy 2025;247:123034. https://doi.org/10.1016/j.renene.2025.123034.
[49] MATLAB H. Version 23.2. 0 (R2023b) 2023.
[50] Lemmon EW, Bell IH, Huber ML, Mclinden MO, Tomassetti S, Di Nicola G, et al. NIST Standard Reference Database 23: Reference Fluid Thermodynamic and Transport Properties-REFPROP, Version 10.0, National Institute of Standards and Technology. Glob Ozone Res Monit Proj 2019;122:23.
[51] Abouzied AS, Samad S, Singh PK, Janabi AH, Shaban M, Mohammed AAA, et al. Waste heat harness in a thermal energy system using TEGs, and SCO2brayton cycle driven by renewable sources for electricity and liquid hydrogen production: Thermo-Economic optimization using ANNs. Case Stud Therm Eng 2025;72:106369. https://doi.org/10.1016/j.csite.2025.106369.
[52] Balali A, Asadabadi MJR, Mehrenjani JR, Gharehghani A, Moghimi M. Development and neural network optimization of a renewable-based system for hydrogen production and desalination. Renew Energy 2023;218:119356. https://doi.org/10.1016/j.renene.2023.119356.
[53] Chitgar N, Sadrzadeh M. Optimizing sustainable energy systems: a comparative study of geothermal-powered desalination for green hydrogen production. Desalination 2025;593:118219. https://doi.org/10.1016/j.desal.2024.118219.
[54] Chitgar N, Moghimi M. Design and evaluation of a novel multi-generation system based on SOFC-GT for electricity, fresh water and hydrogen production. Energy 2020;197:117162. https://doi.org/10.1016/j.energy.2020.117162.
[55] Razmi AR, Alirahmi SM, Nabat MH, Assareh E, Shahbakhti M. A green hydrogen energy storage concept based on parabolic trough collector and proton exchange membrane electrolyzer/fuel cell: Thermodynamic and exergoeconomic analyses with multi-objective optimization. Int J Hydrogen Energy 2022;47:26468–89. https://doi.org/10.1016/j.ijhydene.2022.03.021.
[56] Korpeh M, Asadbagi P, Afshari R, Rashidi A, Lotfollahi A. A comprehensive analysis and multi-objective optimization of a sustainable production system based on renewable energies. Appl Therm Eng 2024;242:122483. https://doi.org/10.1016/j.applthermaleng.2024.122483.
[57] Singh PK, Basem A, Dara RN, Shaban M, Samad S, Ghandour R, et al. Waste heat recovery cycles integration into a net-Zero emission solar-thermal multi-generation system; Techno-economic analysis and ANN-MOPSO optimization. Case Stud. Therm Eng 2025;66. https://doi.org/10.1016/j.csite.2024.105690.
[58] Chitgar N, Karami P, Hemmati A, Sadrzadeh M. A multi-carrier energy system for electricity, desalinated water, and hydrogen production: Conceptual design and techno-economic optimization. Renew Energy 2025;243:122556. https://doi.org/10.1016/j.renene.2025.122556.
[59] Miao Z, Meng X, Li X, Liang B. Influence weights of key parameters and optimization strategies for non-contact thermoelectric generator performance enhancement. Energy 2025;339:139120. https://doi.org/10.1016/j.energy.2025.139120.
[60] Li G, Xu J, Liu S, Zhao D, Zheng Y, Guo W. High-energy density micro swirl combustion powered thermoelectric generator for combined heat and power supply. Therm Sci Eng Prog 2025;68:104369. https://doi.org/10.1016/j.tsep.2025.104369.
[61] Sun L, Basem A, Alhumaid S, Ayadi M, Dahari M, Alharbi T, et al. Thermal energy integration and optimization in a biomass-fueled multi-generation system for power, hydrogen, and freshwater production. Case Stud Therm Eng 2025;76:107394. https://doi.org/10.1016/j.csite.2025.107394.
[62] El-Dessouky HT, Ettouney HM. Fundamentals of Salt Water Desalination. Elsevier 2002. https://doi.org/10.1016/b978-0-444-50810-2.x5000-3.
[63] Berstad D, Skaugen G, Wilhelmsen Ø. Dissecting the exergy balance of a hydrogen liquefier: Analysis of a scaled-up claude hydrogen liquefier with mixed refrigerant pre-cooling. Int J Hydrogen Energy 2021;46:8014–29. https://doi.org/10.1016/j.ijhydene.2020.09.188.
[64] Bouzgarrou S, Abed AM, Chauhan BS, Alsenani TR, Alharbi FS, Alkhalaf S, et al. Thermo-economic-environmental evaluation of an innovative solar-powered system integrated with LNG regasification process for large-scale hydrogen production and liquefaction. Case Stud Therm Eng 2024;53:103904. https://doi.org/10.1016/j.csite.2023.103904.
[65] Ben SM, Basem A, Hasan MA, Le LT, Khlifi MA, Islam S, et al. Exergoeconomic analysis and optimization of a thermal–thermochemical system integrating biomass gasification and geothermal energy for power, methanol, and liquefied hydrogen. Appl Therm Eng 2026;287:129438. https://doi.org/10.1016/j.applthermaleng.2025.129438.
[66] Lotfollahi A, Korpeh M, Balali A, Moghimi M. A sustainable biomass-powered multi-generation system utilizing hydrogen energy storage: Techno-economic-environmental analysis and deep learning-assisted optimization. Energy 2026;342:139706. https://doi.org/10.1016/j.energy.2025.139706.
[67] Kazemi H, Lotfollahi A, Moghimi M. A net-zero carbon emission multi-generation system for green ammonia production: Comprehensive analysis and ANN-assisted optimization using moth flame optimizer. Int J Hydrogen Energy 2025;137:303–22. https://doi.org/10.1016/j.ijhydene.2025.04.510.
[68] Lotfollahi A, Jabraeelzadeh A, Mehrenjani JR, Gharehghani A, Korpeh M. Feasibility study and techno-economic optimization of an efficient renewable-based system for round-the-clock energy harvesting using machine learning approaches: a case study in Khaf city. Int J Hydrogen Energy 2024;50:659–80. https://doi.org/10.1016/j.ijhydene.2023.10.321.
[69] Zuo Z, Wang J, Alghassab MA, Adnan Othman N, Almadhor A, Alhomayani FM, et al. Heat Re-process approach and thermally integrated renewable energy system for power, compressed hydrogen, and freshwater production; ANN boosted optimization and techno-enviro-economic analysis. Case Stud Therm Eng 2025;66:105748. https://doi.org/10.1016/j.csite.2025.105748.
[70] Al-Sulaiman FA, Hamdullahpur F, Dincer I. Performance assessment of a novel system using parabolic trough solar collectors for combined cooling, heating, and power production. Renew Energy 2012;48:161–72. https://doi.org/10.1016/j.renene.2012.04.034.
[71] Ioroi T, Yasuda K, Siroma Z, Fujiwara N, Miyazaki Y. Thin film electrocatalyst layer for unitized regenerative polymer electrolyte fuel cells. J Power Sources 2002;112:583–7. https://doi.org/10.1016/S0378-7753(02)00466-4.
[72] Sharqawy MH, Zubair SM, Lienhard JH. Second law analysis of reverse osmosis desalination plants: an alternative design using pressure retarded osmosis. Energy 2011;36:6617–26. https://doi.org/10.1016/j.energy.2011.08.056.
[73] Ziapour BM, Saadat M, Palideh V, Afzal S. Power generation enhancement in a salinity-gradient solar pond power plant using thermoelectric generator. Energy Convers Manag 2017;136:283–93. https://doi.org/10.1016/j.enconman.2017.01.031.
[74] Maryami R, Dehghan AA. An exergy based comparative study between LiBr/water absorption refrigeration systems from half effect to triple effect. Appl Therm Eng 2017;124:103–23. https://doi.org/10.1016/j.applthermaleng.2017.05.174.
[75] Sengupta M, Habte A, Xie Y, Lopez A, Gueymard CA. The national solar radiation data base (NSRDB) for CSP applications. AIP Conf Proc 2019;2126:51–60. https://doi.org/10.1063/1.5117712.